The Cryosphere, 16, 2373–2402, 2022 https://doi.org/10.5194/tc-16-2373-2022 © Author(s) 2022. This work is distributed under the Creative Commons Attribution 4.0 License.





Snowfall and snow accumulation during the MOSAiC winter and spring seasons

David N. Wagner^{1,2}, Matthew D. Shupe^{3,4}, Christopher Cox^{3,4}, Ola G. Persson^{3,4}, Taneil Uttal³, Markus M. Frey⁵, Amélie Kirchgaessner⁵, Martin Schneebeli¹, Matthias Jaggi¹, Amy R. Macfarlane¹, Polona Itkin^{6,7}, Stefanie Arndt⁸, Stefan Hendricks⁸, Daniela Krampe⁸, Marcel Nicolaus⁸, Robert Ricker⁸, Julia Regnery⁸, Nikolai Kolabutin⁹, Egor Shimanshuck⁹, Marc Oggier¹⁰, Ian Raphael¹¹, Julienne Stroeve^{12,13,14}, and Michael Lehning^{1,2}

Correspondence: David N. Wagner (david.wagner@slf.ch)

Received: 23 April 2021 – Discussion started: 26 April 2021

Revised: 5 February 2022 - Accepted: 20 May 2022 - Published: 17 June 2022

Abstract. Data from the Multidisciplinary drifting Observatory for the Study of Arctic Climate (MOSAiC) expedition allowed us to investigate the temporal dynamics of snowfall, snow accumulation and erosion in great detail for almost the whole accumulation season (November 2019 to May 2020). We computed cumulative snow water equivalent (SWE) over the sea ice based on snow depth and density retrievals from a SnowMicroPen and approximately weekly measured snow depths along fixed transect paths. We used the derived SWE from the snow cover to compare with precipitation sensors installed during MOSAiC. The data were also compared with ERA5 reanalysis snowfall rates for the drift track. We found an accumulated snow mass of 38 mm SWE between the end of October 2019 and end of April 2020. The initial SWE over first-year ice relative to second-year ice increased from 50 % to 90 % by end of the investigation period. Further, we found that the Vaisala Present Weather Detector 22, an optical precipitation sensor, and installed on a railing on the top deck of research vessel *Polarstern*, was least affected by blowing snow and showed good agreements with SWE retrievals along the transect. On the contrary, the OTT Pluvio² pluviometer and the OTT Parsivel² laser disdrometer were largely affected by wind and blowing snow, leading to too high measured precipitation rates. These are largely reduced when eliminating drifting snow periods in the comparison. ERA5 reveals good timing of the snowfall events and good agreement with ground measurements with an overestimation tendency. Retrieved snowfall from the ship-based K_aband ARM zenith radar shows good agreements with SWE of the snow cover and differences comparable to those of ERA5. Based on the results, we suggest the K_a -band radarderived snowfall as an upper limit and the present weather detector on RV Polarstern as a lower limit of a cumulative snowfall range. Based on these findings, we suggest a cumu-

¹WSL Institute for Snow and Avalanche Research SLF, Davos, Switzerland

²CRYOS, School of Architecture, Civil and Environmental Engineering, EPFL, Lausanne, Switzerland

³NOAA Physical Science Laboratory, Boulder, CO, USA

⁴Cooperative Institute for the Research in Environmental Sciences, University of Colorado Boulder, Boulder, CO, USA

⁵British Antarctic Survey – Natural Environment Research Council, Cambridge, UK

⁶UiT – The Arctic University of Norway, Tromsø, Norway

⁷Cooperative Institute for Research in the Atmosphere, Colorado State University, Fort Collins, CO, USA

⁸Alfred-Wegener-Institut, Helmholtz-Zentrum für Polar- und Meeresforschung, Bremerhaven, Germany

⁹Arctic and Antarctic Research Institute, St. Petersburg, Russia

¹⁰International Arctic Research Center, University of Alaska Fairbanks, Fairbanks, AK, USA

¹¹Thayer School of Engineering, Dartmouth College, Hanover, NH, USA

¹²Centre for Earth Observation Science, University of Manitoba, Winnipeg, Canada

¹³Earth Sciences Department, University College London, London, UK

¹⁴National Snow and Ice Data Center, University of Colorado, Boulder, CO, USA

lative snowfall of 72 to 107 mm and a precipitation mass loss of the snow cover due to erosion and sublimation as between 47 % and 68 %, for the time period between 31 October 2019 and 26 April 2020. Extending this period beyond available snow cover measurements, we suggest a cumulative snowfall of 98–114 mm.

1 Introduction

Snow cover on sea ice has many significant effects on the ice mass balance and general heat exchange processes between the ocean and the atmosphere (Wever et al., 2020). As snow will cover almost all Arctic sea ice by the beginning of the melt season and with albedo values close to 0.9, a large amount of the incoming solar radiation is reflected rather than absorbed into the snowpack. Due to its potentially very high insulating capacity, snow acts as an inhibitor for heat transfer between ocean, sea ice and atmosphere (Holtsmark, 1955; Maykut and Untersteiner, 1971; Sturm et al., 2002b). Depending on the season, accumulation, density and thermal conductivity of the snow, the sea ice growth and melt vary temporally and spatially. For instance, the underlying sea ice might undergo faster (slower) growth in autumn when the snow on top is relatively thin (relatively thick). On the other hand, a thicker (thinner) snow cover might lead to delayed (earlier) sea ice melt in the melt season. Consequently, the small-scale snow distribution - which we define in the following as decimetre- to hectometre-scale snow cover area - affects the ice mass balance on the same scales, as large amounts of snow are accumulated along ridges or dunes, while large areas of level ice experience little snow accumulation (Lange and Eicken, 1991; Sturm et al., 1998b; Iacozza and Barber, 1999; Leonard and Maksym, 2011; Trujillo et al., 2016). The snow that has fallen to the ground as fresh precipitation often gets re-distributed as blowing or drifting snow due to the relatively high average horizontal wind velocities during the Arctic winter. The high snow transport rates are also a result of the relatively low aerodynamic roughness length of sea ice, where z_0 is typically lower for first-year ice (FYI) than for second- or multi-year ice (SYI or MYI) (Weiss et al., 2011). In addition, large parts of the snow mass can be expected to get blown into leads or undergo sublimation (Déry and Yau, 2002; Déry and Tremblay, 2004; Leonard and Maksym, 2011; Liston et al., 2020), which has recently been shown to be underestimated by current models (Sigmund et al., 2022). Besides thermodynamic ice growth at its bottom, snow can directly contribute to ice formation on top of the sea ice as snow ice. Snow-ice formation occurs when snow first transforms into slush due to surface flooding of saltwater or direct brine expulsion through thin ice followed by subsequent refreezing (Sturm et al., 1998a; Toyota et al., 2011; Jutras et al., 2016; Sturm and Massom, 2016). The relative mass contribution of snow ice towards sea ice by the end of the accumulation season depends strongly on location, with an approximated average of 6%–10% for Arctic sea ice and with estimated local peaks of up to 80% (Merkouriadi et al., 2020). As a further term in the snow mass balance, Webster et al. (2021) mention sea ice dynamics. However, we can only imagine that the dynamics, such as ridge formation, can lead to a snow mass decrease when the snow is pushed below the ice or into the water.

Considering all effects as snow mass source and mass sink, we can write the mass balance equation of snow over sea ice, modified from the general mass balance description of snow (e.g. King et al., 2008), as

$$\frac{\mathrm{d}M}{\mathrm{d}t} = P \pm E_{\mathrm{s}} \pm E_{\mathrm{e}} - E_{\mathrm{D}} - R + B - I - \nabla \cdot D - L - S, \tag{1}$$

where $\frac{dM}{dt}$ is the rate of change of the mass of the snow cover over the sea ice at one point in kg m⁻², which is equivalent to snow water equivalent (SWE) per time unit; P is the snowfall rate; E_s is the sublimation rate and E_e is the evaporation rate of the snow cover; E_D is the drifting and blowing snow particle sublimation rate; R is runoff; R is brine mass infiltration rate into the snow cover from below; R is the snow-ice formation rate; R is the horizontal snow transport rate of blowing and drifting snow; R is the rate of the snow mass blown into leads; and R is the mass of snow pushed or dug under the ice due to sea ice dynamics. Considering a larger area (i.e. above hectometre scale up to a scale of the whole Arctic ice pack), all terms must be considered, while some terms may become zero when considering the equation at one point; e.g. where no open lead is existent at a point, R becomes zero.

The first and largest source term in Eq. (1) is, depending on the considered area, P. The central Arctic has a dry climate, and depending on location, a yearly average snowfall of approximately 100 to 350 mm can be expected in this area (Serreze and Hurst, 2000; Chung et al., 2011; McIlhattan et al., 2020; Webster et al., 2021). During polar night, the mass decrease in the snow cover by sublimation (E_s) and evaporation (E_e) as well as the mass increase due to deposition (re-sublimation) and condensation can probably be assumed negligible (Liston et al., 2020; Webster et al., 2021). However, sublimation and evaporation terms become larger by the beginning of summer in May and stay relatively large until September. Reliable values from literature are hard to determine, but the snow cover decrease as a combination of $E_{\rm s}$ and D (as snow particles that get lifted into suspension) may be up to 50% (Essery et al., 1999). To estimate the blowing snow sublimation E_D , Chung et al. (2011) applied the sophisticated PIEKTUK blowing snow model (used often and in various forms; e.g. Déry et al., 1998; Déry and Yau, 1999, 2002; Déry and Tremblay, 2004; Leonard et al., 2008; Leonard and Maksym, 2011) for a SHEBA (Surface Heat Budget of the Arctic Ocean) field experiment (Uttal et al., 2002) site, drifting between 74° and 81° N. They computed 12 mm of SWE blowing snow sublimation over a time period of 324 d between November 1997 and September 1998. As

179 mm of precipitation was found for the same time period, the blowing snow sublimation mass sink was 6 % of the total cumulative snowfall. During the Canadian Arctic Shelf Exchange Study (CASES) overwintering campaign, Savelyev et al. (2006) found a relative humidity of over 95 % most of the time and concluded on very low blowing snow sublimation rates. Liston et al. (2020); however, suggested a significant mass reduction of the snow cover by 20 % due to blowing snow sublimation based on modelling results. Within the melt season in summer, R can be expected to be the largest mass sink (Webster et al., 2021). Considering brine infiltration, B, which is often accompanied by the expression of frost flowers, Nghiem et al. (1997) found a 4 mm slush layer forming beneath frost flowers in indoor experiments. However, when snow falls onto frost flowers or a layer of brine, it gets soaked by brine, transformed into slush and, when cold enough, is often transformed quickly into snow ice. Hence, we assume that brine only can be a positive mass term as long as a certain ambient temperature is not undercut, where the snow begins to transform into snow ice. Regarding mass decrease due to snow-ice formation I, Merkouriadi et al. (2020) give an average value of less than 0.05 m snow-ice thickness for the central Arctic. It is hard to estimate a precipitated amount of SWE from recalculation from 0.05 m, as the process of snow-ice formation is complex (Jutras et al., 2016). However, when we assume 0.05 m as snow height with an average fresh snow density of $100 \,\mathrm{kg} \,\mathrm{m}^{-3}$, we expect around 5 mm of SWE decrease, which would mean only about 3 %, relative to the measured 179 mm during SHEBA. The snowice formation rate is expected to be highest in the months of September, October and November (Webster et al., 2021). On one hand, the largest sink term in Eq. (1) is the erosion outside the melting season, represented as D in the mass balance equation, which may make up to 50 % SWE decrease over sea ice of the total precipitated snow mass (Leonard and Maksym, 2011). On the other hand, locally, the eroded mass may deposit at the windward and leeward sides of ridges, on level areas such as dunes, and fill frozen leads - hence locally very often exceeding the precipitated mass. The amount of drifting and blowing snow that is lost and gets melted in open leads L varies strongly depending on location, considered area, ice dynamics and lead properties such as width and orientation relative to the wind. However, the total vanished mass flux from the column of blowing and drifting snow can be locally up to 100 % (Déry and Tremblay, 2004; Leonard and Maksym, 2011). Déry and Tremblay (2004) computed an annual blowing snow loss of 20 mm SWE for a 10 km fetch using the blowing snow model PIEKTUK with a mean lead width of 100 m, an open water fraction of 1 % and a typical lead trap efficiency of 80 %. However, in this model setup, saltation mass flux is not considered. Leonard et al. (2008) and Leonard and Maksym (2011) were doing computations with the same model base for Antarctic sea ice, but considering saltation mass flux in addition. They emphasize the relative importance of saltation mass flux in the compu-

tation, as they find that all saltated mass flux blown towards an open lead vanishes there. They also emphasize that although the mass flux within the saltation layer in their model is lower than in the blowing snow column above, the higher frequency of saltation (about 50 % on 23 d in October 2007) compared against blowing snow frequency makes the mass loss due to saltation an important term. However, only a very limited number of studies were carried out that investigate this specific problem, and the saltation layer with relative large snow mass flux has not been considered in great detail so far. Hence, the existing estimates go along with large uncertainties.

As we will only consider the accumulation time period, we can omit runoff R from Eq. (1). Further, snow cover evaporation and sublimation terms are negligible during this time; hence we can neglect the terms $E_{\rm s}$ and $E_{\rm e}$. Then we write the simplified mass balance equation for winter and early spring as

$$\frac{\mathrm{d}M}{\mathrm{d}t} = P \pm D - L - E_{\mathrm{D}} - I - S. \tag{2}$$

To investigate all effects of the snow cover over the ice – the insulating effect, the sea ice mass contribution effect and the albedo effect – light must be shed into the snow processes that are represented, and detailed knowledge of the evolution of total snow mass $\frac{dM}{dt}$, or SWE over time on top of the ice, is required. However, due to logistical challenges, especially for the winter and spring months, snowfall rate and snow accumulation estimates could only be roughly approximated so far. The past estimates mostly made use of rare point measurements, or rather old time series (Petty et al., 2018) and satellite remote sensing (Petty et al., 2018; Cabaj et al., 2020), leading to high uncertainties in weather, climate and snow cover models as well as in reanalyses. Batrak and Müller (2019), for instance, could show that a 5 to 10 °C warm bias of the sea ice surface temperature in weather forecasts and reanalyses is due to a missing snow layer modelled on top of the sea ice. For snowfall rates and mass balance estimations, some general problems occur: limited data about snowfall rates from precipitation gauges currently exist for this region. Buoys that measure snow height with acoustic sensors which record long continuous time series along its drift tracks throughout the central Arctic do exist (Nicolaus et al., 2021a). However, uncertainties with point snow measurements arise in those windy regions due to the snow transport processes described above. If using precipitation sensors, the high average horizontal wind velocities make snowfall rate estimates difficult for both weighing gauges (Goodison et al., 1998) and optical sensors (Wong, 2012). The wind itself may lead to an undercatch for weighing bucket gauges (Goodison et al., 1998), while blowing snow may lead to overestimation for both weighing gauges and optical sensors (Sugiura et al., 2003). Blowing snow typically occurs at heights up to 10 m, while it can even reach several hundreds of metres in altitude (Budd et al., 1966; Scarchilli et al., 2009). Hence, we expect that blowing snow can often be falsely detected as precipitation by snowfall sensors (Sugiura et al., 2003). Some issues caused by the wind can be corrected with scaling factors or transfer functions, but these need to be identified for these specific conditions (Goodison et al., 1998). Another approach is to measure the snow water equivalent (SWE) of the snow cover. From this, one can derive snowfall rates. However, especially during the polar night, the precipitated snow is dry, and as already indicated above, the wind speed is often sufficiently high to drift the freshly fallen snow particles away immediately. Hence, single point measurements are not appropriate to estimate snowfall, and horizontal sampling distance and temporal distance between sampling days should be kept as short as possible. This becomes more crucial the windier the location is.

During the year-long Multidisciplinary drifting Observatory for the Study of Arctic Climate (MOSAiC) expedition, during which the research vessel (RV) Polarstern (Alfred-Wegener-Institut Helmholtz-Zentrum für Polar- und Meeresforschung, 2017) served as a base moored on two different ice floes, data of snow on the ice as well as of in situ snowfall were collected in great detail for almost the whole MOSAiC period (October 2019–October 2020) (Nicolaus et al., 2021b; Shupe et al., 2022). The dataset includes measurements of the penetration force into the snowpack with a SnowMicroPen (SMP) (Schneebeli and Johnson, 1998; Schneebeli et al., 1999) from which snowpack densities can be estimated (Proksch et al., 2015) as well as bulk SWE measurements, weekly repeated transects of snow depth measurements and a set of precipitation sensors installed on the ice (Vaisala Present Weather Detector 22 (PWD22) (Vaisala, 2004; Kyrouac and Holdridge, 2019), OTT Pluvio² pluviometer (Bartholomew, 2020a; Wang et al., 2019b), OTT Parsivel² (Bartholomew, 2020b; Shi, 2019) and on board RV *Polarstern* (Vaisala PWD22, OTT Parsivel²).

This paper investigates the snow accumulation period from October 2019 to May 2020, where precipitation is solid, and no significant snowmelt was observed. For this period, the intentions in this paper are as follows.

- Compute reliable values for SWE evolution along the fixed transect paths that include surface heterogeneities.
- Use the computed SWE for periods where no drifting snow occurred to compare with snowfall rates from precipitation gauges installed during the MOSAiC expedition and make a best estimate of total precipitation during the investigation period.
- Evaluate an existing radar reflectivity–snowfall (Z_e –S) relationship (Matrosov, 2007; Matrosov et al., 2008) for the ship-based K_a -band ARM zenith radar (KAZR).
- Evaluate the ERA5 (Hersbach et al., 2020) mean snowfall rates for the MOSAiC drift track.

Investigate average snow mass balance and discrepancies of computed snowfall rates and SWE on the sea ice and shed light on the processes described in Eq. (2), such as total eroded mass.

Section 2 introduces our methods, followed by Sect. 3, where we show the results. In Sect. 4 we discuss our results, and in Sect. 5 we draw conclusions about our findings and give an outlook about potential future work.

2 Data and methodology

All data used for evaluations in the following were collected during the MOSAiC campaign (Krumpen et al., 2020; Nicolaus et al., 2021b; Shupe et al., 2022) from the beginning of Leg 1 (24 October 2019) until the end of Leg 3 (7 May 2020) (Fig. 1). On 4 October 2019, RV *Polarstern* moored along an ice floe that originated in the Siberian shelf (Krumpen et al., 2020).

2.1 Ice conditions and central observatory

According to Krumpen et al. (2020), the floe where RV Po*larstern* moored had a size of approximately $2.8 \,\mathrm{km} \times 3.8 \,\mathrm{km}$ and was a loose assembly of pack ice little less than a year old that had survived the 2019 summer melt. Figure 2 shows a map of the ice and snow surface structures and installations by 5 March 2020 of the MOSAiC central observatory. Note that the shown elevation range is only approximate as problems occurred with the inertial navigation system of the laser scanner. This led to tilts, and the single swaths within the map have staggered heights. At present, these uncertainties could not yet be corrected. However, very bright areas indicate ridges of around 2 m height, with locally 3 m height and more. The central observatory (all installations in the close vicinity of *Polarstern*) was distinguished from the distributed network, which consisted of remote autonomous stations at least a few kilometres away from the CO. The detailed concept of the central observatory and distributed network is explained in Nicolaus et al. (2021b). The core of the floe consisted mostly of deformed second-year ice (SYI), and the ice surrounding this core mainly consisted of frozen melt ponds (remnant SYI) and partially first-year ice (FYI). When the ship moored, the heading of RV Polarstern was about 220° in October 2019. Significant changes in ice conditions occurred the first time around 16 November 2019, when a storm led to strong ice deformations in and around the CO. Another significant ice deformation event occurred around 11-12 March 2020 and periodically until 7 May 2020. Over time, the floe rotated anticlockwise and reached a minimum heading of 75° on 21 March 2020.

We describe the measuring setup and the post-processing for all used data streams in the following.

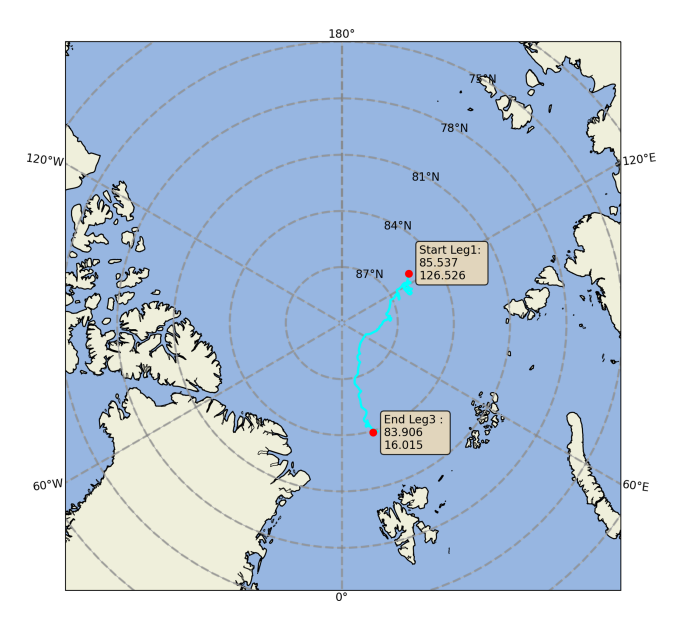


Figure 1. The drift trajectory of RV *Polarstern* between 24 October 2019 and 7 May 2020.

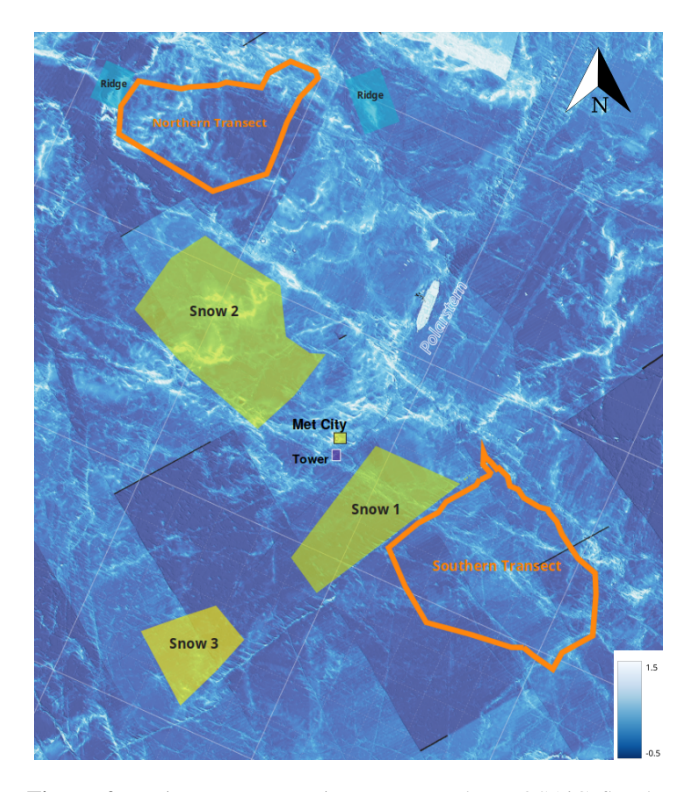


Figure 2. Main snow measuring areas on the MOSAiC floe by 5 March 2020. The bottom layer is a digital elevation map (DEM) from airborne laser scanning (ALS) with the helicopter. The square side length of the underlay grid is 500 m. The transect paths and margins of the shaded measuring areas are based on GPS measurements. The legend for elevation is shown in metres. However, the elevation range is only approximate due to issues with the inertial navigation system which could not be corrected as of yet.

2.2 Snow cover measurements

2.2.1 SMP force and SWE measurements

We measured snow water equivalent (SWE) with an ETH tube, a SWE sampler that is commonly used in Switzerland (Haberkorn, 2019; López-Moreno et al., 2020), as well as resistance force with the SnowMicroPen (SMP) (Schneebeli and Johnson, 1998; Schneebeli et al., 1999) and snow height at different sites (areas shaded in yellow in Fig. 2). The bulk SWE measurements with the ETH cylinder follow the simple principle where the mass of the snow fitting in a tube with a known cross-sectional area is weighed on a spring scale, which yields the SWE in millimetres or $kg m^{-2}$. The device is calibrated for low temperatures, which is most important for the steel spring of the scale. López-Moreno et al. (2020) made an intercomparison of various bulk density and SWE samples including the ETH tube and tested for instrumental bias and variability. It can be concluded that from a single ETH tube measurement we might expect a maximum error of 10%. This value appears high, but given the fact that the average Arctic sea ice snow cover is thin, the absolute error will be low. Given a 20 cm snow depth, the maximum expected error would only be 2 cm. López-Moreno et al. (2020) also argue that particularly light samples may lead to an additional 10% of error with respect to the weighing process with the spring scale itself. Nonetheless, a currently nonquantified error is that during a bulk SWE measurement a sharp transition between snow cover and sea ice often cannot be determined, which is especially valid for an underlying surface scattering layer (SSL) on SYI. However, we use a relatively big sample size of n = 195 bulk SWE measurements, and with increasing sample size, uncertainties are expected to be increasingly levelled out. To avoid wind influence on the measurements, the weighing was conducted in the wind shadow of surrounding objects, surrounding persons or the person measuring.

The SMP is a device which measures the penetration resistance force (*N*) by means of a rod with a conic tip that is slowly driven vertically into the snowpack. A force sensor is connected to the tip which detects the force that is needed to drive into the snowpack with micrometre resolution. The output is given as a force–snow depth signal. These penetration resistance force signals can be used to estimate snowpack density and detect the layers in the snowpack (Proksch et al., 2015; King et al., 2020). We used three different sensors, but all SMP version 4, during MOSAiC. Processing of density from SMP force signals is discussed in the next section.

The map in Fig. 2 shows the floe state on 5 March 2020, which changed significantly due to ice dynamics that started on 11 March 2020. Snow was measured at the different sites as well as along both transect loops. The measurements cover a large area of the floe, including level, remnant SYI, FYI and deformed SYI. Details about the sampling procedure will follow below. Snow 1 was characterized mainly by a mixture

of remnant SYI and deformed SYI. In the beginning, Snow 1 was mostly flat, but the surface became rougher over the time of the expedition. At Snow 1 we deployed three snow pit sites, which were maintained until the end of leg 3. The Snow 2 plot was characterized as an open level field, mostly on remnant and deformed SYI with a distinct high and long pressure ridge in the centre of the plot. On Snow 2, we maintained two snow pit locations until the end of leg 3. Both sites had very similar underlying ice conditions. Snow 3 was created at a later point, furthest away from the vessel. In the beginning, it was a very flat area with underlying FYI and was maintained during leg 3 but needed to be abandoned due to ice dynamics in mid-March. Further, weekly snow pit measurements were conducted along the south-westerly section of the northern transect loop. Also, transects were conducted infrequently over ridges, and measurements were conducted weekly at the ice coring sites during Leg 1 (beyond the map boundaries in Fig. 2, but located north-west of the ship), among other measuring locations. The large variety of locations, their underlying ice types and snow depths allow us to take the spatial heterogeneities of the snow cover into account. However, since we use a bulk approach with the collected SMP and direct SWE data, detailed information on each measuring site is not needed and will not be provided here.

At the measuring locations, SWE, snow height and penetration resistance force measurements with the SMP were done. The SMP measurements at the recurring snow pit locations were conducted as follows: five SMP measurements were performed at a distance of about 20 cm along a line parallel to the old snow pit wall to account for the spatial heterogeneity of the snowpack. On the ridge sites, for instance, SMP measurements were conducted infrequently as transects over ridges. We used these measurements to estimate SWE along the northern and southern transect loops, which will be explained below. For more details about the SMP and SWE collection, we refer to Macfarlane et al. (2021, 2022), Wagner et al. (2021) (data publicly accessible after the end of the MOSAiC moratorium in January 2023) and soon-to-bepublished data and method papers by MOSAiC participants that describe the MOSAiC snow measurement setup in detail.

2.2.2 Transects

Snow depth transects were conducted weekly with a Magnaprobe (Sturm and Holmgren, 2018; Itkin et al., 2021), if the atmospheric, ice or overall safety conditions did not prevent it. The transect path was distributed into two loops (Fig. 2): a northern loop, mostly situated on deformed SYI, and a southern loop, which was mainly situated on FYI and remnant SYI with underlying frozen melt ponds. A transition zone distinguished these two loops, mostly consisting of frozen melt ponds with a very flat surface without significant heterogeneities. The approximate ice conditions and the transition and the transition of the second conditions and the transition of the second conditions and the second conditions and the transition of the second conditions and the second conditions and the second conditions are second conditions.

sect loop locations can be seen in orange on the MOSAiC floe map from 5 March 2020 (Fig. 2). The elevations on the southern transect are mostly below around 1 m height. The elevations are generally higher on the northern transect, although it does not cover ridges of up to 3 m height or more as they have been observed on the Snow 2 plot. One important aspect to note is that surrounding elevations of the ice (i.e. ridges) often exceed the height of the transect areas, for instance in the north and the south of the northern transect or in the north and the east of the southern transect. The expected result from this surrounding sea ice characteristic is that during drifting snow events, snow might get caught upwind of the transect areas, while wind speeds may decrease, potentially leading to flow separation and a bias in the total snow accumulation. We consider this a non-quantifiable uncertainty at this point of research. The only way to overcome this problem in the future is to cover larger sampling areas and increase the number of these. To find an optimum between technical effort and reliable result, one could decrease these areas until average values are not changing any more significantly.

The GPS coordinates of the Magnaprobe were transformed into coordinates of a local metric coordinate system, called "FloeNavi" (Fig. 3). Furthermore, the transects were partially corrected for shifts within the ice, which was especially the case for an event with strong ice dynamics on 16 November 2019. Thus, the southern loop transects until (including) 14 November 2019 are marked as a yellow rectangle in Fig. 3. Note that a part of the northern transect was off the regular transect track on 31 October 2019, which leads to some uncertainties in evaluations. However, we tested how it affected the average when only the off track was cut off versus the whole northern transect. We found an increase of only 0.8 mm when the whole track was considered. Hence, though this leads to some uncertainties, we included the 31 October 2019 transect for further evaluations. For all other days of sampling, though the transects may deviate from one another within the FloeNavi coordinate system, the actual transect path was the same. After the coordinate transformation and horizontal correction, for good spatial and temporal comparability, clear margins as shown in the rectangles in Fig. 3 were defined for the "southern" and "northern" transect loops. By the overlays, one can recognize that the transect loops were not significantly impacted by internal differential ice movements.

However, ice dynamics affected the transects, especially from 11/12 March 2020 on, where leads and cracks opened throughout the paths. Overall, we tried to minimize the influence of these ice deformation events on the transect measurements. However, an impact on the time series cannot be excluded. On the transects, snow height measurements were sampled with the Magnaprobe with an average distance between measuring points of 1.1 m. Note that this value is simply an average that contains the uncertainty of GPS localization, coordinate transformation and the step length of

the user, while the users varied mainly between each leg of MOSAiC. The average distance between measurements was computed after applying the FloeNavi coordinate transformation. Values $z < 0.00\,\mathrm{m}$ as well as $z > 1.40\,\mathrm{m}$ (the technically constrained measurable length) were discarded as incorrect data. In this study, we did not account for further corrections that may come along with a tip sinking into material below the snow cover, for instance the surface scattering layer on SYI. Sturm and Holmgren (2018) showed that this error is hard to quantify, as it depends strongly on the ground material and of course the applied force as well – an issue which also occurs for crusts within the snow cover. Similar issues occur for other snow measurements, such as the ETH tube and SMP, as well, which will be mentioned later in the text again.

The northern loop was sampled from 24 October 2019 to 7 May 2020 on 24 d with an average path length of 954 m. The southern loop was sampled from 31 October 2019 to 26 April 2020 14 times with an average transect path length of 974 m. More in-detail data and instrument description are found in Itkin et al. (2021).

To take surface roughness (i.e. variability of snow surface height) and potential snow accumulation at surface irregularities better into account, we looked at the weekly snow height differences of the transects. With the given average horizontal sampling distance (1.03–1.21 m), no small-scale patterns are considered (sastrugi, for instance) for evaluation. However, since the extent of ridges and most types of dunes are larger than 1.2 m in all horizontal directions(Filhol and Sturm, 2015), we expect our typical horizontal sampling scale to accurately characterize the spatial distribution of accumulation, which we demonstrate in Sect. 2.3.1.

2.3 SMP density retrievals and SWE from transect snow depths

Based on how the campaign was planned, we have considerably more SMP force measurements available (N=3007) than bulk SWE weighing measurements (N=195). Furthermore, for each snow pit we made at least n=5 SMP measurements, and the SMP was often used even for ridge transects; these measurements best characterize the spatial heterogeneity in the snow depth across the sea ice. Not many direct SWE measurements or SMP force measurements are available along the transect path. Hence, we use the direct SWE measurements for validation but apply a statistical SWE–snow depth (HS) relationship to estimate SWE along the full path (Sturm et al., 2002a; Jonas et al., 2009).

Snowpack density can be estimated with a statistical model from SMP snow depth–force signal profiles (Proksch et al., 2015):

$$\rho = a + b \ln \left(\tilde{F} \right) + c \ln \left(\tilde{F} \right) L + dL, \tag{3}$$

where a (kg m⁻³), b (N⁻¹), c (N⁻¹ mm⁻¹) and d (mm⁻¹) are empirical regression coefficients; \tilde{F} is the median pen-

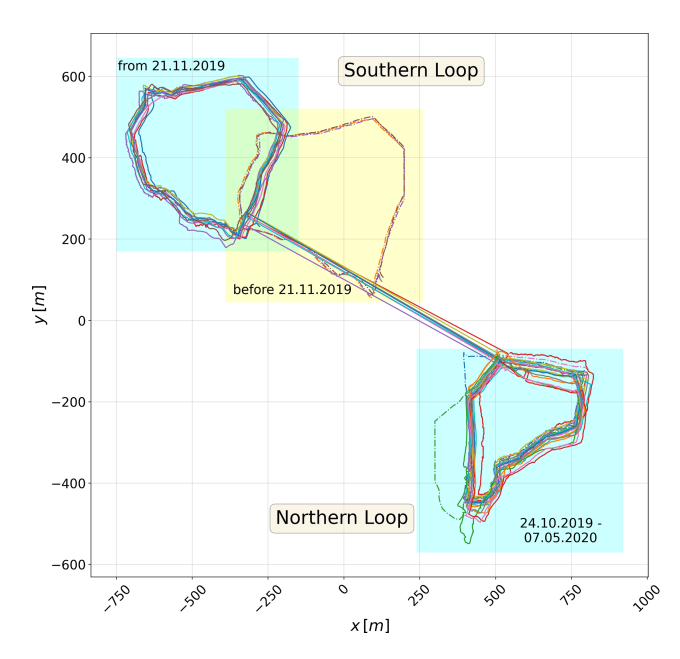


Figure 3. Magnaprobe transect paths with coordinates transformed to the FloeNavi grid corrected for ice drift. The rectangles represent the margins that were used as a definition for the "northern transect loop" (upper left) and "southern transect loop" (bottom right) for good comparability. The shifts between transect paths within a rectangle originate from corrections and coordinate transformation, though the actual transect paths were the same.

etration force of the SMP (N) for a specified sliding window; and L is the microstructural length scale (Löwe and Herwijnen, 2012) for the same window. Both \tilde{F} and L are computed for the window size of 2.5 mm with a 50 % overlap, which is the same as used in Proksch et al. (2015), but contrary to Calonne et al. (2020) (1 mm) and King et al. (2020) (5 mm). King et al. (2020) calibrated the corresponding coefficients to snow on Arctic sea ice and found a = $315.61 \,\mathrm{kg} \,\mathrm{m}^{-3}$, $b = 46.94 \,\mathrm{N}^{-1}$, $c = -43.94 \,\mathrm{N}^{-1} \,\mathrm{mm}^{-1}$ and $d = -88.15 \,\mathrm{mm}^{-1}$. The coefficients show a significant improvement in density derivation for snow on sea ice, which is reflected by the decrease in the root-mean-square error (RMSE) (Proksch et al. (2015): RMSE = 130 kg m^{-3} ; King et al. (2020): RMSE = 41 kg m^{-3}) without removing outliers, compared against density cutter measurements. Consequently, we used the coefficients from King et al. (2020) for the following SWE computations. From the SMP density estimates we can compute

$$SWE = HS \cdot \overline{\rho}, \tag{4}$$

where HS (m) is the height of snow over the ice or snow depth, and $\overline{\rho}$ (kg m⁻³) is the vertically averaged density of the snowpack. The computed SWE dataset is documented in detail by Wagner et al. (2021). Similar to Jonas et al. (2009), but applying the function directly to SWE, we fitted the following function to the available bulk SWE measurements as

well as SWE retrievals from the SMP:

$$SWE = m \cdot HS^a, \tag{5}$$

where m is the fitted slope and a is a fitting coefficient. For the bulk SWE measurements, we found m = 334.61 and a = 1.14 (Fig. 4). For the SMP retrievals we found m = 323.97 and a = 1.07. As we have more SMP measurements available in total, and especially for deep snow depths compared with the ETH tube, we computed SWE based on fitted SMP density–SWE parameters as

$$SWE = 323.97 \cdot HS^{1.07}.$$
 (6)

From Fig. 4 one can clearly see that the improvement for snow on sea ice of the coefficients found by King et al. (2020) is valid for MOSAiC legs 1-3 SMP data, too (Fig. 4c) and that the coefficients determined by Proksch et al. (2015) and Calonne et al. (2020) appear not appropriate to estimate SWE of snow for this MOSAiC period. Furthermore, the lowest RMSE (expressed here as average error of individually computed SWE relative to the regression line for an individual parameter setup) was found for the fitted model with the coefficients from King et al. (2020) (7.2 mm SWE) compared against 15.4 mm (Proksch et al., 2015) and 9.4 mm (Calonne et al., 2020). However, one should note the following limitations in this comparison: first, we used a sliding window size of 2.5 mm for all computations, which is the same as in Proksch et al. (2015), while Calonne et al. (2020) used 1 mm and King et al. (2020) 5 mm. However, the strength of the influence can be at least partially invalidated by the fact that Calonne et al. (2020) state that they tested for sensitivity of three different window sizes of 1, 2.5 and 5 mm and could not find a significant influence on the result - which is not quantified in the publication. At least choosing a fixed window for each parameterization – as we did with the 2.5 mm window – increases the comparability. Another limitation might be that the Proksch et al. (2015) calibration was made with a SMP version 2, while we, Calonne et al. (2020) and King et al. (2020) use the newest SMP version 4.

We applied our fitted formula to each snow depth measurement with the Magnaprobe along the transect path to obtain the SWE estimates. The SWE was rounded to integers for the following description in the text, except when two values that are compared are very similar. No rounding was conducted before any computations. The average computed SWE will also serve as a reference comparison with snowfall sensors and ERA5 as described in Sect. 2.8.

A limitation with this approach is that different snow layers are not distinguished by density, even though a wind-packed layer has a higher density than a depth hoar layer. Hence, when high winds lead to drifting snow deposition that is detected by a snow height increase with the Magnaprobe, the SWE increase is likely to be underestimated, as would be the eroded mass of a drifting snow layer. It is beyond the scope of this study to attempt an approach that distinguishes

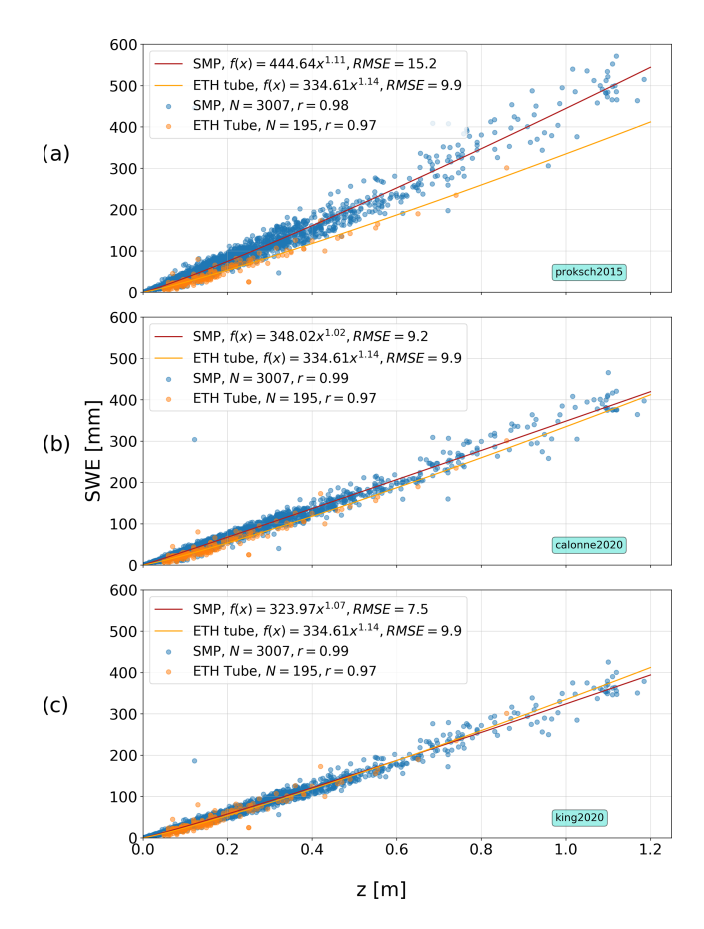


Figure 4. Scatter plots and fitted HS-SWE function of SMP derived SWE and measured SWE with the ETH tube for **(a)** the density computation coefficients from Proksch et al. (2015), **(b)** Calonne et al. (2020) and **(c)** King et al. (2020).

different snow layers. Instead, for validation, we compared SMP and ETH tube measurements with transect-computed SWE along a section of the northern transect loop for 14, 21 and 28 November 2019 (Fig. 5). The validation measurements were conducted at different positions at each day of measurements and contain drift locations and level ice areas. Note that this quantitative comparison of bulk SWE and SMP SWE versus transect contains uncertainties as the accuracy of GPS measurements (2 m) and the following coordinate transformation of the Magnaprobe as well as the SMP coordinates do not allow for centimetre-scale precision. Further, the pits were dug up to a vertical distance of 1 m from the transect path, in order to sample fresh snow that is not disturbed by repeated transects. For quantitative comparison, SWE computations from direct bulk SWE and SMP measurements along the transects were plotted over SWE model retrievals. Figure 5a shows the measuring locations for each SMP measurement along the northern transect loop (five measurements at each snow pit location), and Fig. 5b-d show the corresponding SWE plotted over the x axis of the FloeNavi for different days of measurements.

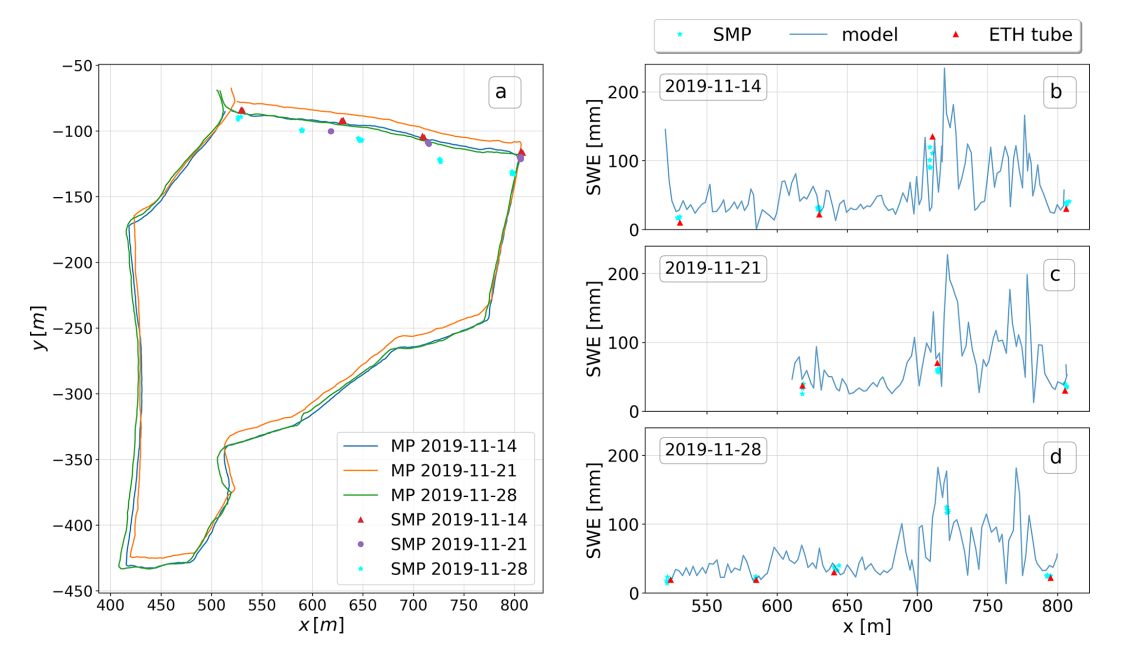


Figure 5. (a) SMP measurement locations along the Magnaprobe (MP) transect path on 14 (2019-11-14), 21 (2019-11-21) and 28 November 2019 (2019-11-28). The GPS coordinates were transformed into local FloeNavi grid coordinates. Panels (**b**), (**c**) and (**d**) show the comparison of SWE estimates from direct SMP measurements, direct bulk SWE measurements and SWE derived with the HS-SWE model from the Magnaprobe snow depth measurements along the northern transect as *x*-axis location on the FloeNavi grid, for 14, 21 and 28 November 2019.

This comparison shows that the modelled SWE matches the derived SWE from SMP retrievals and bulk SWE measurements quite well during the three chosen time periods, even for higher SWE estimates, where a higher scatter is expected (Fig. 4). Note that although the time distance between the 3 d of measurements is relatively short, we found that 42 % of the time for drifting snow conditions the threshold friction velocity for snow transport was exceeded (the lower snow particle counter (SPC) was not installed yet at this time) from and including 14 November until and including 21 November 2019. From and including 21 November until and including 28 November 2019 the threshold was exceeded 57% of the time. This means we can expect redistributed snow for the 2d following 14 November. Intercomparing SMP SWE versus ETH SWE, we find a RMSE of 16.3 mm for 14 November, 8.1 mm for 21 November and 3.5 mm for 28 November. However, we must note that the depth of SWE measurements from the ETH tube and SMP has some individual but differing restrictions: firstly, as the SMP cut-off force signal was set to 40-41° N (depending on the device), the snow depth was determined whenever one of those values was reached, which is not necessarily the snowice interface. Secondly, during the sampling period, there was no method established to distinguish between surface scattering layer (SSL) and snow. Hence, its vertical position was determined visually, which was not always clear. Therefore, a measurement with the ETH tube might or might not include the surface scattering layer which formed during the melt season of 2019. If the SMP was able to penetrate the SSL only partially while it was not measured with the ETH tube, then SWE is overestimated from the SMP measurements. Otherwise, if the SMP could not penetrate the SSL while it was partially measured with the ETH tube, the SMP-based SWE computation overestimates actual SWE. However, as the SMP SWE retrievals are often close to the direct SWE measurements, one can assume reliable values on the whole. Research to determine exact boundaries between snow and sea ice is ongoing. Furthermore, since the number of measurement points along a transect is large and we do not expect systematic biases, we believe that fluctuations caused by these various sources of uncertainty will largely average out, such that the results from the applied SWE model yield a reasonable estimate along the transect.

Under Appendix A we make a comparison with derived SWE over Arctic sea ice during the SHEBA campaign conducted by Sturm et al. (2002a) in a similar manner. The comparison shows the difference between their and our results and underlines the importance of using our approach for MO-SAiC snow cover data.

2.3.1 Evaluating the sensitivity of the arithmetic mean with respect to horizontal sampling distance

As shown by Trujillo and Lehning (2015), a sufficiently small sampling interval of point measurements is crucial for estimating representative values of spatially averaged snow depths. We studied the sensitivity of the horizontal sampling interval for average mass estimates by reducing the sample

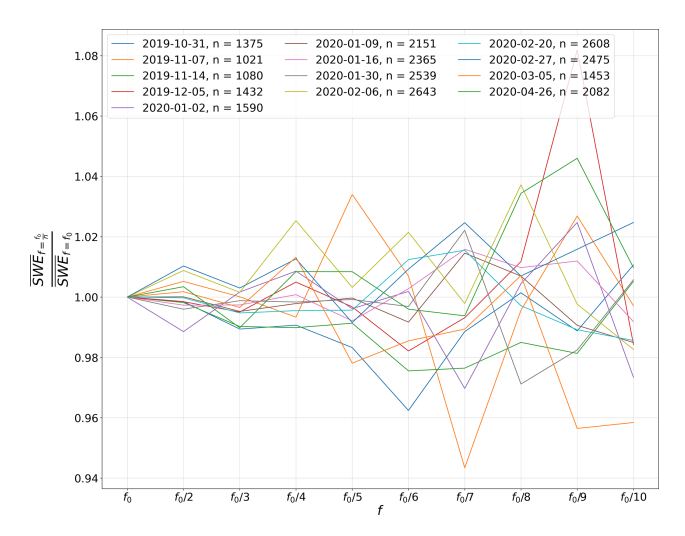


Figure 6. Sensitivity of the transect average as a factor of the Magnaprobe horizontal sampling. The x axis shows the horizontal transect sampling frequency in relation to the original sampling frequency f_0 , and the y axis shows the ratio of the average SWE of all tested frequencies to the average SWE of the original sampling frequency for each day of sampling (31 October 2019 to 26 April 2020).

numbers from using all samples (Magnaprobe average sampling distance of 1.1 m) down to considering every 10th sample (about 11 m sample distance) for the average. The process was conducted for each day of sampling, and the averages were normalized against the original sampling frequency (Fig. 6).

The results show that for sampling frequencies down to one-third of the original frequency (sampling distances ranging from 1.1 to 3.4 m) the average mass estimates vary by less than ± 1 %. This indicates that a sampling distance up to 3.4 m is mostly robust and that no significant undersampling occurred. This also shows that the impact of variations in sampling interval distance that inevitably occurs with different operators of the Magnaprobe is probably negligible. The larger fluctuations in computed average mass for longer sample interval distances suggests undersampling at those scales and less reliable averages. However, a validation of uncertainties that could accompany varying vertical penetration force leading to different measured snow height, e.g. when a crust within the snow is penetrated or not due to varying operators, is not conducted here. The operators were aware of this issue and tried to apply a similar power for the Magnaprobe sampling.

2.4 Snowfall rates

2.4.1 Precipitation gauges

Snowfall rates were estimated using standard internal processing software from five distinct precipitation gauges operated by the US Department of Energy Atmospheric Radiation Measurement (ARM) program. Two sensors investigated here were installed on the railing on the top deck of Polarstern - a Vaisala Present Weather Detector 22 (Vaisala, 2004; Kyrouac and Holdridge, 2019) (referred to as PWD22PS in the following) and an OTT Parsivel² laser disdrometer (Shi, 2019; Bartholomew, 2020b) (referred to as P2PS in the following) (Table 1). The PWD22PS was installed at 22 m and the P2PS at 24 m above the water line. On the ice, in "met city" (Fig. 2, in the following, referred to as MC), three precipitation sensors were installed: (1) an OTT Parsivel² (P2MC), installed at 1.5 m nominal height above the snow surface, surrounded by a double-alter shield; (2) a PWD22 (PWD22MC), installed at 2 m nominal height, unshielded; and (3) an OTT Pluvio² L (Wang et al., 2019b; Bartholomew, 2020b), shielded by a double-alter shield and installed at 1 m above the snow (referred to as Pluvio2 in the following). Different ARM data levels of the devices are given, where a1 means "calibration factors applied and converted to geophysical units" and b1 means "QC checks applied to measurements".

Optical devices evaluated here are the Vaisala PWD22 and the OTT Parsivel². However, the measurement technique and the process of estimating snowfall rates are different. The Parsivel² is a laser disdrometer that processes the voltage signal changes due to light extinction when a hydrometeor falls through the laser beam. It has an effective measuring area of 54 cm² to estimate hydrometeor size and velocity (Löffler-Mang and Joss, 2000). The hydrometeors are classified into size classes which can be used to investigate the particle size distribution. The precipitation type is determined by deviceinternal spectral signature comparison, where the spectra are determined empirically. Based on particle size, velocity and estimated precipitation type, device-internal software computes a snowfall estimate. No details are known about the exact formula used by the manufacturer for the snowfall estimate. Its accuracy is given by the manufacturer as $\pm 20\%$ with an intensity range of 0.001 to $1200 \,\mathrm{mm}\,\mathrm{h}^{-1}$ (Table 1). The calibration was conducted in the manufacturer's laboratory, and therefore no calibration was needed in the field.

The PWD22 consists of several sensors that are used to compute the snowfall rate: the two core sensors are a transmitter-receiver combination, where the transmitter emits pulses of near-infrared (NIR) light. The receiver on the other side measures the scattered part at 45° of the light beam from the emitted signal (sampling volume 100 cm³). Rapid changes in the scatter signal between transmitter and receiver are used to compute precipitation intensity. The sampling volume allows for the detection of single crystals and aggregates of snow crystals (snowflakes). Furthermore, the PWD22 is equipped with a heated RAINCAP rain sensor, which produces a signal proportional to the amount of water on the sensing element. By means of the ratio from sample volume and water content determined with the RAINCAP sensor, precipitation types are distinguished. In the tube between the transmitter and receiver, another temperature sensor (thermistor) is installed. The detected temperature is used to select the default precipitation type. When frozen precipitation is detected, the PWD22 software multiplies optical intensity with a scaling factor, determined from RAINCAP and optical intensities from the receiver to estimate snowfall intensity as SWE per time unit (Vaisala, 2004). The manufacturer does not provide a value for accuracy; however the intensity measuring range is given as 0.00 to 999 mm h⁻¹. There is no calibration principle known for the field, but the manufacturer mentions comparisons with close reference gauges as a calibration method.

The only device that we compare here that uses a weighing principle is the OTT Pluvio². The instrument's core is a sealed load cell that continuously measures the weight of the precipitation falling into the entry of the bucket. The installed variant was an OTT Pluvio² L Version 400, with a collecting area of $400\,\mathrm{cm^2}$ and a recording capacity of 750 mm of precipitation. Its accuracy is given by the manufacturer as $\pm\,0.1\,\mathrm{mm\,min^{-1}}$ or $\pm\,6\,\mathrm{mm\,h^{-1}}$, or $\pm\,1\,\%$, and its intensity range is given as $\pm\,6\,\mathrm{mm\,h^{-1}}$ or 0.1 to 30 mm h⁻¹. No calibration for the OTT Pluvio² is needed in the field as it was delivered calibrated by the manufacturer. However, calibration weights were used to test for accuracy.

The data streams were downloaded from the ARM data archive (https://adc.arm.gov/, last access: 14 June 2022) and scanned for quality control flags. Values with timestamps that correspond to flags indicating maintenance time or suspicious or incorrect values were discarded.

2.4.2 Snowfall retrievals from the Ka-band ARM zenith radar

Snowfall was retrieved from the K_a -band ARM zenith radar (KAZR) (Widener et al., 2012; Lindenmaier et al., 2019) that was installed on a container at the bow of RV *Polarstern*. Using a radar snowfall retrieval allows us to investigate snowfall continuously and eliminates impacts on gauges such as acceleration effects of wind that result in undercatch or overestimation due to blowing snow particles. The KAZR operated at approximately 35 GHz. We computed the snowfall rate S (mm h^{-1}) according to the power law

$$Z_{e} = a S^{b}, (7)$$

where Z_e (mm⁶ m⁻³) is the radar equivalent reflectivity factor, and a and b are empirical coefficients. We chose a = 56 and b = 1.2 as these were found to be good average values for dry snowfall at this radar frequency, and no significant riming was observed (Matrosov, 2007; Matrosov et al., 2008).

Near-field radar measurements can suffer from a variety of issues, such that snowfall retrievals typically must be applied to radar signals that are elevated above the surface. To find an appropriate KAZR range gate to extract snowfall rates, we plotted the cumulative sums of SWE based on KAZR-derived snowfall from reflectivity measurements at different

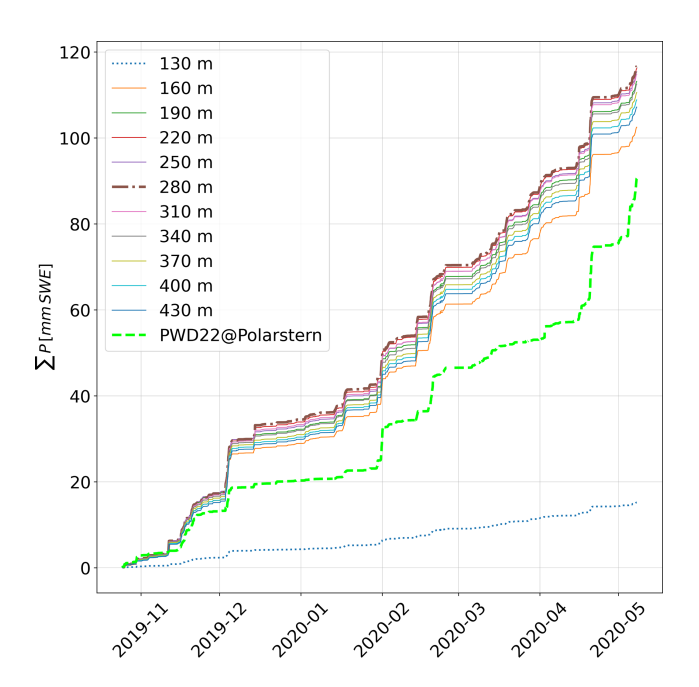


Figure 7. Computed cumulative snowfall for different KAZR range gates and PWD22PS.

range gates (Fig. 7). The first range gate of 100 m did not yield any measurements, while at 130 m reflectivities were too low. From Fig. 7 we see that the differences in the cumulative snowfall from range gates between 220 and 280 m are the least. The decrease in computed snowfall with height beyond 280 m is probably due to very low cloud heights in winter (Jun et al., 2016), such that snowfall would get underestimated as these range gates are often at higher elevations within the clouds or even beyond the cloud top. We found the largest snowfall rates for the 280 m range gate; thus we chose it as the range gate from which we extracted the snowfall retrievals. However, based on this simple analysis, the potential differences in snowfall based on this choice of range gate are on the order of about 10 %. With an instrument elevation of 14 m a.s.l., the elevation of the extracted snowfall rates is 294 m a.s.l.

2.5 Atmospheric flux station data

A meteorological tower of $10 \,\mathrm{m}$ height was installed on the ice $558 \,\mathrm{m}$ away from RV *Polarstern* at about 60° off the bow of the vessel in the middle of October 2019. However, due to ice dynamics, by the end of leg 3 (beginning of May 2020), the distance was only about $334 \,\mathrm{m}$ while the direction from the ship stayed approximately the same (Fig. 2). At nominal levels z=2, 6 and $10 \,\mathrm{m}$ above the snow, three-dimensional wind (u,v,w) and temperature were measured at high frequency with METEK uSonic-3 Cage MP anemometers (METEK GmbH, 2022), while on the same elevation levels, relative humidity and temperature were measured with Vaisala HUMICAP humidity and tem-

Table 1. Summary of validated installed precipitation sensors and radar during MOSAiC as well as details about the ERA5 reanalysis (PS: RV *Polarstern*, MC: met city, DA: double-alter shield, WL: water line, DFIR: double fence intercomparison reference).

ERAS	OTT Pluvio ²	OTT Parsivel ²	Vaisala PWD22	KAZR	OTT Parsivel ²	Vaisala PWD22		Device/reanalysis
I	MC	MC	MC	PS	PS	PS		Loc
1	Pluvio2	P2MC	PWD22MC	KAZR	P2PS	PWD22PS		Abbreviation
1	I (Snow)	1.5 (Snow)	2 (Snow)	14 (WL)	24 (WL)	22 (WL)	Snow/WL (m)	Nominal height
1	DA	DA	I	ı	1	1		Shield
Hersbach et al. (2020)	Wang et al. (2019b)	Shi (2019)	Kyrouac and Holdridge (2019)	Lindenmaier et al. (2019)	Shi (2019)	Kyrouac and Holdridge (2019)		Data reference
1	al	b1	b1	al	61	ь1	data level	ARM
1	$\pm 6 \mathrm{mm} \mathrm{h}^{-1}$ $\pm 0.1 \mathrm{mm} \mathrm{min}^{-1}$ $\pm 1 \%$	±20%	İ	I	±20 %	1	1	Accuracy
1	6–1800 mm h ^{–1}	$0.001{-}1200\mathrm{mm}h^{-1}$	$0.00-999\mathrm{mm}\mathrm{h}^{-1}$	ı	$0.001-1200 \mathrm{mm}\mathrm{h}^{-1}$	0.00–999 mm h ⁻¹		Intensity range
+62.8 mm cum. SWE/snow buoys (Wang et al., 2019a); slight underestimate in summer/CloudSat (Cabaj et al., 2020); overestimate in other months	-63 % from median (max)/DFIR; -14 % from median (min)/DFIR (Wong, 2012)	See above	See above	23 % relative bias/ shielded Nipher gauge (Matrosov et al., 2008)	+46 %/+54 % from median/DFIR (Wong, 2012); +24 %/+29 % from median/DFIR (Wong et al., 2012)	-32 % from median/DFIR; (Wong, 2012) +33 % from median/- manual (Boudala et al., 2016)	,	Selected existing snowfall validations/ reference setup
1	Manufacturer/calib. weights	Manufacturer	Reference comparison	ı	Manufacturer	Reference comparison		Calibration

perature HMT330 sensors (Vaisala, 2009). The University of Colorado/NOAA surface flux team carried out the post-processing and computed turbulent fluxes, such as momentum flux and turbulent heat fluxes, mixing ratio, or friction velocity. Wind vectors were corrected; i.e. processed wind directions are according to geographic true north. We used wind velocity, wind direction, computed latent heat flux, friction velocity, relative humidity, the temperature at 2 m and temperature of the snow surface from the described dataset (Cox et al., 2021).

2.6 Drifting and blowing snow mass flux

On the meteorological tower described under Sect. 2.5, two snow particle counters (SPCs) (Sato et al., 1993) were installed. The devices continuously detect number and sizes of snow particles which are transported through a laser beam. The devices rotate with very low friction on a vertical axis, and mounted wind vanes at the back of the sensor keep the laser beam 90° towards the wind. One SPC was installed at about 0.1 m (SPC1104) and one at 10 m (SPC1206) above the snow. The lower SPC1104 ran with only a few interruptions from 2 December 2019 until 7 May 2020 (data availability for this period 96.6%). The upper SPC1206 ran with only a few interruptions from 14 October 2019 until 7 May 2020 (data availability for this period 94.9%). One bigger data gap for the SPC1206 was between 17 November 2019, 03:05:00 UTC and 18 November, 11:15:00 UTC because there was a power interruption due to sea ice dynamics resulting in broken power lines. Note that the SPC1206 data at 10 m are still under quality control, and the absolute mass flux values have some error yet to be quantified. Regardless, the comparison between the two SPCs yields an order of magnitude of the mass flux and its relative change at 10 m compared to near the surface at 0.1 m.

To determine periods where snow transport and erosion have occurred, horizontal mass flux $(kg m^{-2} s^{-1})$ for both SPCs was computed as (Sugiura et al., 2009)

$$Q_{\text{SPC}} = \frac{\pi \,\rho_{\text{p}}}{6} \sum_{n=1}^{64} S_n \,N_n \,D_n^3, \tag{8}$$

where ρ_p is the density of a drifting snow particle, which we assumed here to be the density of ice $\rho_p = 917 \text{ kg m}^{-3}$; S_n is the shape factor of snow particles of the *n*th class, which we assumed to be 1 here; N_n is the particle flux of the *n*th class (m⁻² s⁻¹), which is the number of particles per class passing the SPC sensor area A_s in a second; and D_n is the diameter of a drifting snow particle of the *n*th class (m).

It is likely that the distance between sensor and snow cover varied over time since installation on 2 December 2019 due to deposition of new snow. In any case, given these uncertainties, to determine potential drifting snow periods for periods where the SPC might fail, the critical friction velocity

for snow particles was calculated as (Bagnold, 1941)

$$u_{*t} = A \cdot \sqrt{\frac{\rho_{\text{ice}} - \rho_{\text{air}}}{\rho_{\text{air}}} g \overline{d}}, \tag{9}$$

where A is a threshold parameter and is here assumed to be 0.18 as found by Clifton et al. (2006) for drifting snow initiation, $\rho_{\rm ice} = 917\,{\rm kg\,m^{-3}}$ is the density of ice, $\rho_{\rm air}$ is the density of air, $g=9.81\,{\rm m\,s^{-1}}$ is gravity acceleration on earth and \overline{d} is an average particle diameter, which we assumed to be 260 µm, which was found as the lowest particle diameter on the surface where snow transport was observed by Clifton et al. (2006). $\rho_{\rm air}$ could be retrieved from the meteorological tower data. The computed thresholds were applied to computed u_* from the tower. If $u_* > u_{*t}$, particles begin to get lifted from the ground, and drifting snow flux is initiated.

The mass decrease computed with the HS-SWE function from the transect is temporally compared against computed cumulative snow mass flux from the snow particle counters. Note that the cumulative horizontal mass flux is only an indicator for the strength of the erosion but cannot be translated into actual eroded mass. To distinguish in the text between computed SWE decrease in the snow cover and cumulative mass flux and to avoid confusion, we keep the designation SWE for the snow cover but use kg m⁻² for cumulative mass flux in the following, although SWE has the same units.

2.7 ERA5 mean snowfall rates

For the drift track coordinates of RV *Polarstern*, shown in Fig. 1, we extracted ERA5 (Hersbach et al., 2020) mean snowfall rates, which are the sum of the convective and large-scale snowfall in ERA5. While the large-scale snowfall is generated from the cloud scheme in the ECMWF Integrated Forecasting System (IFS) (IFS Documentation CY47R1 – Part IV, 2020), the convective snowfall is generated from the IFS convection scheme. The resolution for ERA5 over the sea is $0.28125^{\circ} \times 0.28125^{\circ}$, which is about $31 \, \mathrm{km} \times 31 \, \mathrm{km}$. Hence, the extracted snowfall rate from ERA5 for the drift track does not refer to points but represents an averaged value over these grid cells closest to the drift track coordinates. The purpose here is to compare the ERA5 mean snowfall against snow cover SWE and sensors in this study.

2.8 Sensor and reanalysis comparison method

We computed the average SWE for the northern and southern loops (Table 2) as we expect this combination of deformed SYI, remnant SYI and FYI is more representative for an overall snow accumulation estimate than choosing a snow deposition for one of these ice types. Additionally, in Sect. 3 and Fig. 9 we will show that change of average SWE along a section of the whole transect several hundreds of metres long is over 200 % from the average SWE along the whole northern transect, compared before and after a drifting snow event. This confirms the need for as long of transect sections as possible to find an average snow mass value for an area that can

be representative for the MOSAiC ice floe. Indeed it is impossible to determine at this point with this dataset we made use of whether only the SWE derived from the northern or southern or the average of loops, is the best choice to evaluate snowfall. A snow height difference dataset based on laser scanners of an area that includes both northern and southern transects and an area beyond that could be used to validate transect snow depth. However, we do not make use of such a dataset here. We will demonstrate in the coming sections that initial average SWE on the northern loop is about twice the value of the average SWE on the southern loop.

The SWE increase until January 2020 is much faster on the southern loop; hence, we see a different accumulation rate depending on whether we measure snow depth on SYI (northern loop) or FYI (southern loop). Indeed, what "most representative" means also strongly depends on the horizontal extent of snowfall and wind patterns, i.e. the total accumulated snow mass that has fallen over a certain area but is re-deposited due to wind. This is a problem we are not able to consider in this study but that can potentially be solved by computing snow mass based on the difference of airborne or terrestrial laser-scan-derived heights. The reason why we decided to use an SWE average of the northern and southern loops as reference is that the MOSAiC ice floe consisted in large parts of these two ice types.

This average computed snow cover SWE serves then as our reference for the precipitation sensors and ERA5 snowfall. Note that for the averaging process, data were discarded when only the northern or southern transect loop was measured on 1 d, except when the temporal distance between the measurement of northern and southern loops was short and there was no snowfall in between. This is only the case for 24 (northern) and 26 (southern) April. Hence, the transect averaged SWE starts on 31 October 2019 and ends on 24 and 26 April 2020, with a significant reduction of days of sampling, compared to all days of transect sampling available (Table 2). RMSE between snow cover SWE and sensor- and reanalysis-estimated SWE was computed for the time period where no SWE decrease in between the days of the transect sampling has been detected by means of the computed snow cover SWE, which is all days before and including 20 February 2020. Here we used n = 10 d for subtracting SWE, which results in n = 9 d for error comparison. The RMSE is computed as millimetres and always refers to the precipitation sum between days of transect sampling.

To discuss the erosion influence on potential discrepancies of snow cover SWE and sensor-estimated snowfall in more detail, in addition, RMSE was computed for days after time periods where no significant amounts of horizontal mass flux were detected with the SPCs, i.e. where no erosion between 2 d of transect sampling was expected. These detected drifting snow periods until 20 February were 3–5 December, 19 December 2019, 30 January–2 February and 18–20 February 2020. Hence, in this case, 5 December 2019, 6 February and 20 February 2020 were discarded from trans

sect SWE time series for evaluation; hence $n = 6 \,\mathrm{d}$, which are the days before and after the drifting snow events, were left over for comparison with sensors and ERA5. This results in n = 5 pairs for error calculation. The drifting-snow-free periods are marked as yellow areas in the graph of Fig. 11f. Note that due to the strong cumulative aspect (i.e. we compare snowfall that is always accumulated between the days of transect measurements), the difference is naturally reduced when reducing the sample number. The reduction of validation pairs reduces the significance of the comparison; however, we additionally inter-compare the error change of the sensors and ERA5, which may strengthen the significance considering the role of wind.

3 Results

3.1 Snow mass accumulation and decrease

Figure 8a shows the derived SWE evolution as box-andwhisker plots for the northern and southern transects. The initial average SWE values for the northern loop (66 mm on 31 October) are naturally higher than for the southern loop (32 mm on 31 October), as the northern transect was situated mostly on deformed SYI. The value for the northern loop decreased to 65 mm until 5 December, while average SWE for the southern loop increased by 29 mm to a similar value of 66 mm between 14 November and 5 December 2019. The SWE on both transect loops increased to 92 mm on the northern loop and 80 mm on the southern loop, between 5 December 2019 and 20 February 2020. From then on, there was a decrease observed in both loops, with a minimum of 79 mm on the northern loop on 6 April 2020 and a minimum of 73 mm on the southern loop on 5 March 2020. On both transects, SWE increased afterward, to 90 mm on the northern loop by 24 April 2020 and 81 mm on the southern loop by 26 April 2020. Hence, even though the initial SWE over the remnant SYI and FYI (southern loop) was approximately only half of the value on the northern loop, it reached 90 % of the snow mass of the northern loop by the end of the accumulation period.

In the following, we present detailed results about snow mass decrease. Notably, we find a net mass decrease, computed with the HS-SWE function, of 9.5 mm for the northern transect loop between 27 February and 20 March. The mass increased again to 90 mm between 20 March and 24 April 2020. The maximum on the northern loop is reached with 94 mm on 7 May 2020. This, however, is not comparable with the southern loop as the southern transect time series only last until the end of April 2020. The SWE maximum on the southern loop is found to be 81 mm on 26 April 2020. The time from 20 February to 20 March falls exactly into the period where (1) the discrepancy between cumulative SWE from the precipitation sensors and SWE from the transect becomes large (Figs. 10b, 11a) and

Table 2. Used transect days of sampling and specifications: transect N–S refers to the northern–southern transect; averaged for validation refers to the days when the transect SWE was averaged as shown in Fig. 8; RMSE with drifting snow describes all days when SWE was subtracted from the respective day before, while all days where subtracted in a row; and RMSE without drifting snow/pair refers to the days used for validation when no or low drifting snow mass flux was detected in between while the respective days after which subtraction was performed consecutively are listed as well. The corresponding RMSE values including regression lines are shown in Fig. 12. The comparison with bulk SWE and SMP refers to the dates where direct comparisons are made with SWE along the transect derived from the HS-SWE (Fig. 5).

Date	Transect N-S	Averaged for validation	RMSE with drifting snow	RMSE without drifting snow/pair	Comparison with bulk SWE and SMP
24 Oct 2019	N	-	_	-	_
31 Oct 2019	N-S	yes	yes (start)	_	_
7 Nov 2019	N-S	yes	yes	yes (start)/14 Nov 2019	_
14 Nov 2019	N-S	yes	yes	yes/7 Nov 2019	yes
21 Nov 2019	N	_	_	_	yes
28 Nov 2019	N	_	_	_	yes
5 Dec 2019	N-S	yes	yes	_	_
19 Dec 2019	N	_	_		_
2 Jan 2020	N-S	yes	yes	yes/5 Dec 2019/9 Jan 2020	_
9 Jan 2020	N-S	yes	yes	yes/2 Jan 2020/16 Jan 2020	_
16 Jan 2020	N-S	yes	yes	yes/9 Jan 2020/30 Jan 2020	_
30 Jan 2020	N-S	yes	yes	yes (end)/16 Jan 2020	_
6 Feb 2020	N-S	yes	yes	_	_
20 Feb 2020	N-S	yes	yes (end)	_	_
27 Feb 2020	N-S	yes	_	_	_
5 Mar 2020	N-S	yes	_	_	_
20 Mar 2020	N	_	_	_	_
26 Mar 2020	N	_	_	_	_
30 Mar 2020	S	_	_	_	_
6 Apr 2020	N	_	_	_	_
16 Apr 2020	N	_	_	_	_
24 Apr 2020	N	yes (avg with 26 Apr 2020)	_	_	_
26 Apr 2020	S	yes (avg with 24 Apr 2020)	_	_	_
30 Apr 2020	N	- · · · · · · · · · · · · · · · · · · ·	_	_	_
7 May 2020	N	_	_	_	_

(2) where about 45 % $(1.977 \times 10^6 \text{ kg m}^{-2})$ of the total cumulative horizontal snow mass flux at 0.1 m above the surface over the whole measuring period of the SPC1104 has occurred (Fig. 11f). That means over 45 % of drifted snow mass appeared on only 19 % (30 out of 158) of the days from the whole measuring time of the lower SPC. The period is marked as green shaded areas in Fig. 11. Most distinct in this period was the event on 24-25 February (marked as red shaded areas in Fig. 11), during which $1.014 \times 10^6 \,\mathrm{kg}\,\mathrm{m}^{-2}$ of cumulative mass flux was detected with the lower SPC - which is 23 % of the total detected cumulative mass flux on 1.3 % of the days the device was running. During this storm, a maximum peak of around 11 m s⁻¹ was detected in the 1h averaged wind speed data at 2m above the ice, which means that the measured peak at shorter time intervals must have been higher. We computed the sum of the detected mass decrease that occurred between days of sampling and that is driven by erosion (but does not reflect the total eroded mass) for the northern loop as $\Delta SWE = -24 \text{ mm}$ (between 31 October 2019-26 April 2020) and for the southern loop as $\Delta SWE = -16 \,\mathrm{mm}$ (between 31 October 2019– 24 April 2020). Figure 9 shows the SWE for the same section of the northern loop transect as in Fig. 5 (268 m length), for 20 February and 5 March 2020, which are before and after a drifting snow event. As the section on 5 March had twice the average horizontal Magnaprobe sampling distance compared to 20 February, and for better illustration, a simple moving average with a window of n = 4 was applied to the section on 20 February while a moving average with a window of n=2 was applied to the data from 5 March. A significant re-distribution due to wind is recognizable. During the same period, the average decrease for this section was 12 mm SWE (from 82.6 to 70.1 mm – a relative value of 15%), while for the whole northern loop the average decrease was 8 mm (from 87.3 to 79.5 mm – a relative value of 9%).

Finally, we present results of the average SWE of the northern and southern loop (Fig. 8b). The average initial SWE value on 31 October 2019 was 48 mm and increased

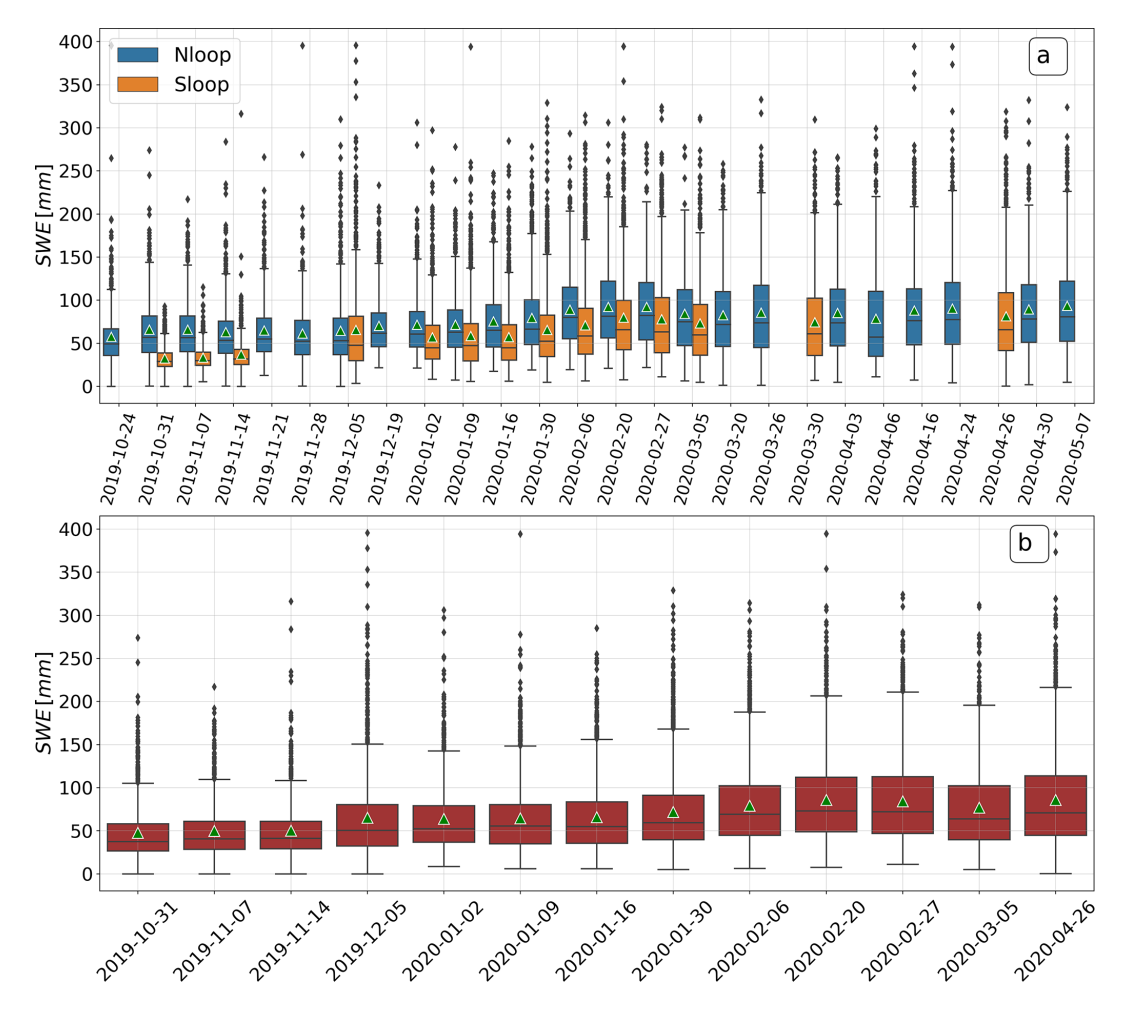


Figure 8. (a) Box-and-whisker plots for SWE estimates along the northern ("Nloop") and southern ("Sloop") transect. **(b)** Box-and-whisker plots for averages of the northern and southern transect loops. Horizontal lines show the median, green triangles the average, the boxes show the interquartile ranges (IQR) (25 %–75 %), and the whiskers represent 1.5 times the upper and lower values of the IQR. The dots represent outliers that are beyond 1.5 times the IQR. Note the different dates between **(a)** and **(b)** as data where only data for one loop were available were discarded for computation of **(b)**. The exception is 24 and 26 April 2020 as the temporal distance was so close that these were averaged, too.

to 86 mm on 24 and 26 April 2020. Hence, we estimate the total mass increase over time as about 38 mm. Over the transect average, the SWE decrease during the snow transport event was 5.5 mm on 24–25 February 2020.

3.2 Precipitation sensor and radar snowfall retrieval comparisons

To compare with the different estimates of snowfall, the cumulative SWE values were examined for each approach. The plot of cumulative snowfall between 31 October 2019 and 7 May 2020 without any corrections applied can be seen in Fig. 10a. The snowfall rates deviate heavily from one another between precipitation data source and locations. The P2PS shows the highest cumulative snowfall, while the P2MC shows the lowest, although with limited data availability (Bartholomew, 2020b). As a result of the limited avail-

ability and wide spread between these two identical systems operating at different locations, we no longer consider the P2MC. The PWD22PS shows the lowest cumulative snowfall with 97.6 mm, while the highest is estimated by the P2PS (290.3 mm). It also stands out that the cumulative sum of ERA5 (110 mm) by 7 May 2020 is very similar to that of the snowfall estimated from the KAZR (114 mm).

Figure 10b compares the northern, southern and average transect loop SWE values with the uncorrected cumulative snowfall from a subset of the sensors and the ERA5 mean snowfall. The PWD22PS is well in line with SWE from the snow cover until the middle to end of February 2020. Afterwards, more snow over the ice was eroded, which is indicated by high horizontal drifting and blowing snow mass flux measured with both SPCs (Fig. 11f). After mid-February, the snow cover SWE did not increase significantly and instead

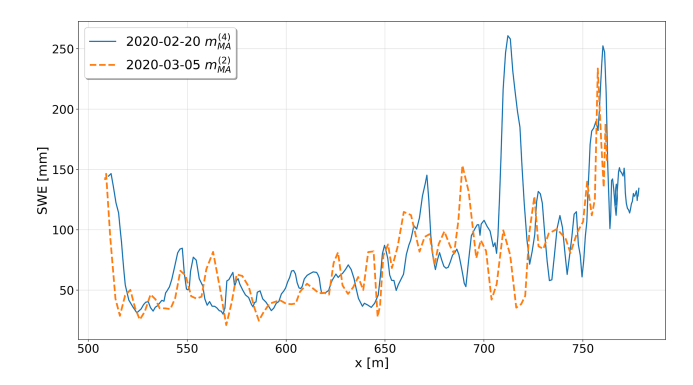


Figure 9. Retrieved SWE from same Magnaprobe section as shown in Fig. 5 on 20 February before a strong drifting snow event that occurred on 24–25 February and mass distribution on 5 March 2020 after the drifting snow event. The superscript numbers in brackets in the legend correspond to the count of numbers of the moving median window used for plotting.

stagnated, while the sensors indicate periodic snowfall. Thus, the discrepancy between sensor snowfall rates and snowpack SWE became larger.

RMSE with respect to SWE difference is shown for snowfall sensors, KAZR and ERA5 (Fig. 12). We consider the case first where snowdrift time periods are included in the evaluation (i.e. all days of sampling until and including 20 February 2020). For this period, a SWE increase in the snow cover of about 37 mm was detected (Fig. 12a, cumulated within the intervals in between $n = 9 \,\mathrm{d}$). Figure 12b, in contrast, shows RMSE computed only for days when no drifting or low drifting snow occurred (n = 6 d). For this time period, an increase of 13.7 mm SWE was detected for the transect. Considering the first case (n = 9 d), all sensors appear to overestimate. However, as expected, this indicates that erosion occurred in the time periods between the days the transects were sampled, which leads to a systematic positive bias of the sensors. For this case the PWD22PS is most similar to the SWE (RMSE = 2.01 mm), followed by ERA5 (3.33 mm), the KAZR (4.65 mm), Pluvio2 (6.7 mm), PWD22MC (8.72 mm) and P2PS (26.39 mm).

However, in the second case ($n = 6 \,\mathrm{d}$), the differences are reduced significantly for all devices and ERA5, too. In this case, Pluvio2 shows the closest comparison to the SWE (RMSE = 1.72 mm). PWD22PS shows good agreement (RMSE = 1.96 mm) with a tendency towards underestimation. It reveals that ERA5 also performs well (RMSE = 2.88 mm), but with an overestimation tendency, as all validation pairs were positively biased with an average of 2.0 mm. Besides ERA5, the KAZR (RMSE = 3.55 mm), systematically positively biased with 2.4 mm, shows the least RMSE decrease compared to the case using $n = 9 \,\mathrm{d}$, which is very likely the result of the fact that both ERA5 and KAZR are not wind-vulnerable in contrast to the other sensors. The

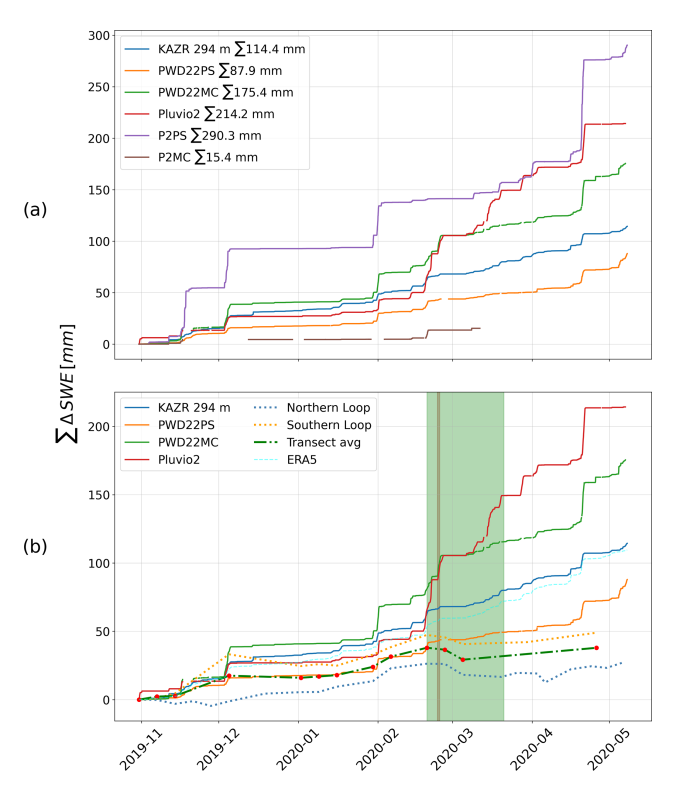


Figure 10. (a) Cumulative snowfall for different installed precipitation sensors during MOSAiC from 31 October 2019 to 7 May 2020. (b) Sensors, ERA5 estimates and SWE of the snow cover. The red dots show the days on which both transect loops were sampled. The red shading shows the time period of the strong drifting snow event on 24–25 February 2020. The green shaded area marks the strong drifting snow period where 45 % of all cumulative horizontal mass flux was detected (Fig. 11).

largest difference of the sensors relative to the snow cover is found for P2PS (RMSE = 3.12 mm).

Note that due to the strong cumulative aspect (i.e. we compare snowfall that is always accumulated between the days of transect measurements), the difference is naturally reduced when reducing the sample number. Nonetheless, the fact that there is an overall tendency towards a decrease in the apparent overestimation of the sensors relative to the SWE indicates that erosion likely did occur before the days eliminated in Fig. 12b. For the PWD22PS, the RMSE is only reduced by about 2.5 %, for ERA5 by 13 % and the KAZR by 23.7 % while for P2PS the RMSE was reduced by 88 % and for PWD22MC reduced by 69 %. For the Pluvio2, the difference was reduced to 26 % of its initial value. While the apparent overestimation of the sensors in Fig. 12a is likely due to erosion (and hence strongly biased), these different magnitudes of RMSE reduction (Fig. 12b) suggest that PWD22PS is less affected by overestimation due to high wind speeds that accompany blowing snow, compared to PWD22MC or Pluvio2, both of which were installed near the surface, but

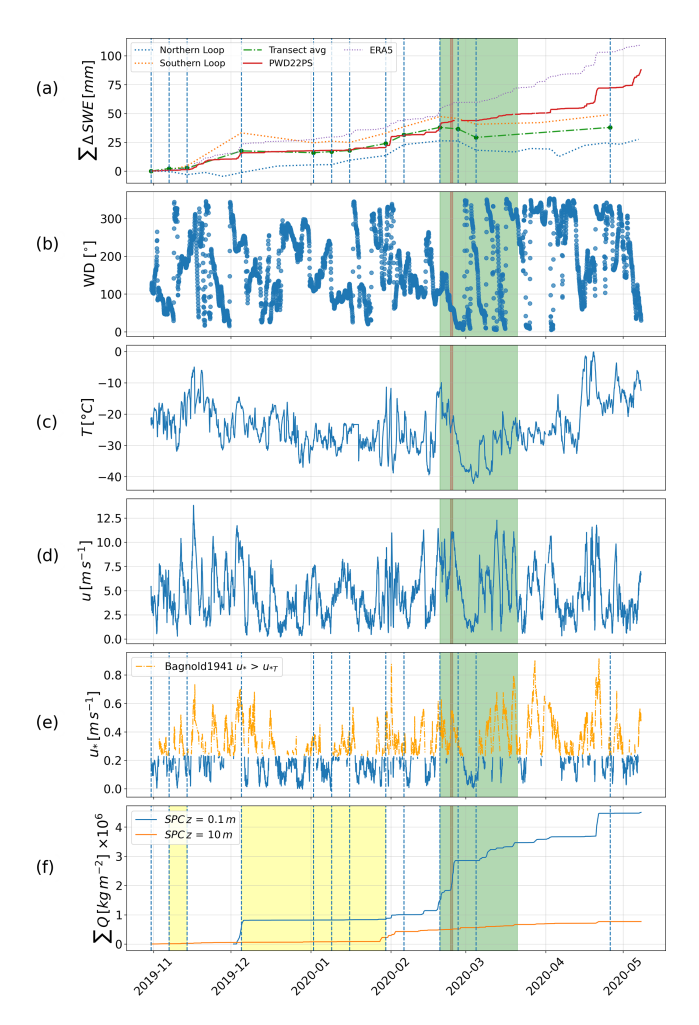


Figure 11. Time series from 31 October 2019 to 7 May 2020 for (a) estimated SWE from the transect and HS-SWE model as well as cumulative snowfall from ERA5, cumulative snowfall from PWD22 on *Polarstern* and KAZR-derived snowfall rates. (b) Wind direction at 2 m, (c) air temperature at 2 m above the snow, (d) wind speed at 2 m height, (e) computed friction velocity threshold for snow transport after Bagnold (1941) and (f) cumulative horizontal mass flux with the snow particle counter at 0.1 m above the snow and at 10 m height. The green shaded areas mark the strong drifting snow period where 45% of all cumulative horizontal mass flux was detected. The vertical blue dashed lines mark the days where both transect loops were sampled. The yellow shaded areas mark the time periods when no to very low mass was detected by means of the snow particle counters.

also compared against P2PS, which is a device known for wind vulnerability towards overestimation of snowfall.

In summary, if we only consider time periods without drifting snow, Pluvio2 and PWD22PS compare most favourably with SWE, however with reasonable results for ERA5, KAZR, PWD22MC and P2PS, as well. When also considering high wind speeds and blowing snow, the PWD22PS still appears to compare most favourably with

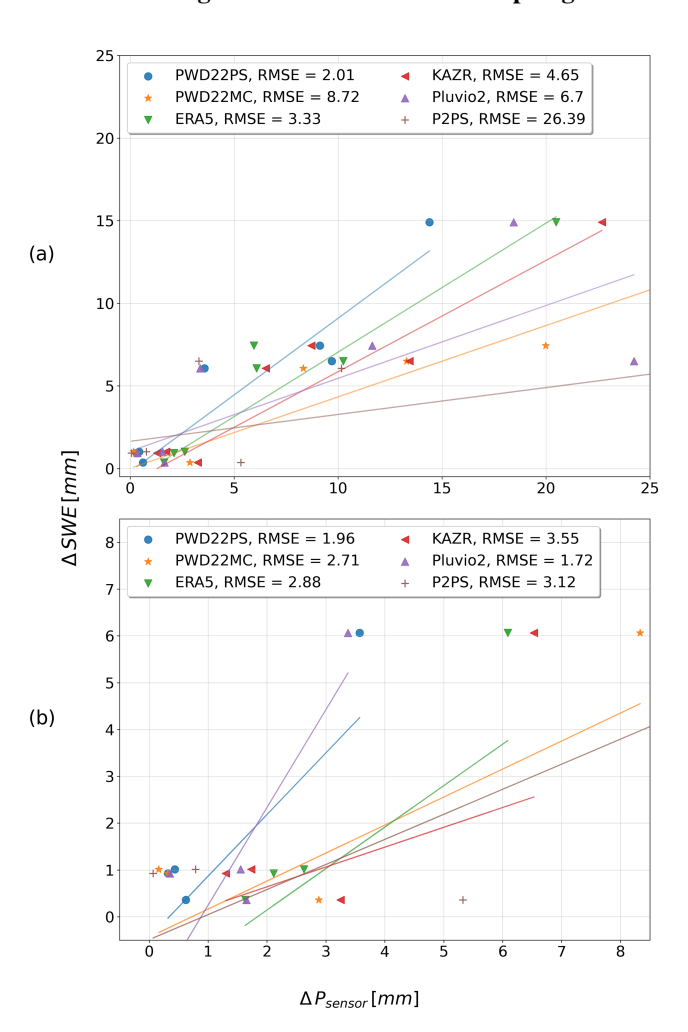


Figure 12. (a) RMSE (mm) of the sensors and ERA5 with respect to snow cover SWE, for the time period before 20 February 2020 with $n = 9 \,\mathrm{d}$ of sampling, including days when drifting snow was detected. Panel (b) is as (a) but without days when drifting snow was detected before $(n = 6 \,\mathrm{d})$. The lines show the linear regression for each sensor.

SWE, while especially P2PS, PWD22MC and Pluvio2 appear to be most negatively affected by high wind speeds.

Taken together, we detected five significant snowfall events. If we use PWD22PS as reference, we find the following for 3–5 December 2019: ≈ 5.5 mm, 30 January–3 February 2020: ≈ 10 mm, 18–21 February 2020: ≈ 8.5 mm, 16–21 April 2020: ≈ 16.5 mm and 4–7 May 2020: ≈ 14 mm. Hence, about 54 mm of snow fell during events, while the other 33 mm fell in between, e.g. as trace precipitation or diamond dust.

To better illustrate the blowing snow influence on sensors that is already suggested by Fig. 12, we made scatter plots of snowfall rates from different sensors with respect to the PWD22PS. Figure 13 shows a scatter plot for the short time of 2 d between 24 and 25 February, where high drifting snow mass fluxes were detected. We can clearly see

that the Pluvio2 (Fig. 13b) and the PWD22MC (Fig. 13d) strongly overestimate snowfall relative to PWD22PS, while P2PS (Fig. 13a) and KAZR (Fig. 13d) stay largely unaffected and only measure trace precipitation of 0.1 to 0.2 mm h⁻¹. This becomes even clearer when we look at snowfall rates of Pluvio2 (Fig. 14a) and PWD22MC (Fig. 14b) versus the horizontal mass flux detected by the SPCs.

Scatter plots for the whole period (31 October 2019–7 May 2020) for different sensors versus horizontal mass flux reveal the influence of drifting and blowing snow, too (Fig. 15). Pearson correlation coefficients show medium positive correlations for mass flux and snowfall from Pluvio2 at SPC height at 0.1 m (Fig. 15b, r = 0.58) and PWD22MC (Fig. 15d, r = 0.55) while a weak negative correlation is observed for P2PS (Fig. 15a, r = -0.2) and for PWD22PS (Fig. 15c, r = 0.26). These results indicate that instruments collocated on the ice at about 1–1.5 m height are much more affected by drifting and blowing snow than instruments installed on *Polarstern* at 22 m height.

We compare ERA5 mean snowfall rates against the snow cover SWE and against PWD22PS. As described above, when we consider the comparisons illustrated in Fig. 12b, ERA5 shows reasonable results with a relatively low RMSE of 2.9 mm and an overestimation tendency. Assuming PWD22PS as reference, ERA5 shows an overall good timing of the snowfall events (Figs. 10b, 11a). As for the transect SWE validation, it overestimates snowfall relative to PWD22PS, too, in this case systematically and with an acceleration of the positive bias from the end of February on. This leads to an overestimation (relative to PWD22PS) of the total accumulation of almost 22 mm (+25 %) by the end of the investigation period. We computed the RMSE for the snowfall rate relative to PWD22PS as 0.06 mm h⁻¹ for the whole time period from 31 October to 7 May 2020.

4 Discussion

4.1 Snow mass balance

With the fitted HS-SWE function, we were able to retrieve the SWE of snow cover over the ice for the transect loops. We could show that comparing the average SWE of a northern loop section with 268 m length (Fig. 9) with the average SWE for the whole northern loop, the SWE change due to a drifting snow event was different by more than 100 %. This shows the need for sampling with large spatial extents which was one reason – besides including both characteristic ice types for the ice floe during MOSAIC, SYI and FYI – why we decided to use the SWE average of both northern and southern loops as a reference for snowfall sensor and reanalysis comparison. Nonetheless, a snow height difference comparison of terrestrial laser scanning (TLS) or airborne laser scanning (ALS) digital elevation models and transect snow depth would be desirable.

For the evaluation of the SWE increase and decrease, note that the net decrease generally includes eroded mass in addition to incoming precipitated mass; hence the eroded mass was often larger than the precipitated mass. These two quantities can only be determined separately when considering snowfall events and no drifting snow events at the same time in between days of sampling.

The constant value of SWE from 20 February on raises the question of a saturation mass of snow that can accumulate in this windy environment, where the roughness of the surface might be a limiting factor. Possibly, this is due to smoothing of the initially rough sea ice surface due to deposited drifting snow. The less rough the surface, the less snow can accumulate. This may also be related to the faster increase in SWE on FYI compared to SYI and the fact that the initial 50 % of SWE over FYI reached 90 % of the SWE over SYI by the end of the investigation period. One hypothesis might be that over SYI the snow mass is rather saturated, as the snow had time to smooth the ridges already over one season before, while FYI might be more rough as long as fresh ridges are existent. Weiss et al. (2011) found in general higher aerodynamic roughness lengths for SYI. With higher roughness length we expect more flow separation and more accumulation. However, the study is more than 10 years old, and given the fact that average ice thickness is thinning in the context of global warming, we might see less stable FYI by the year 2019/2020, resulting in more ice motion and ridge formation – and leading to larger aerodynamic roughness lengths.

It also remains to be investigated why most drifting snow and erosion occurred from 20 February 2020 on, as indicated by transect SWE decrease and horizontal mass flux. Indeed, snow mass flux rates are high until 27 February, but on the sampling day itself, the wind speed as well as the mass flux rate dropped (Fig. 11). Between 27 February and 5 March, the probability for snow transport was very low, indicated by both SPC mass flux and computed threshold friction velocity. One might consider that lower horizontal sampling distance $(D_{5 \,\text{Mar}} = 1.6 \,\text{m})$ could have led to an underestimation of the accumulated snow. However, from Fig. 6 one can see that reducing the sampling frequency by half has no significant effect on the average. One can only see a significant fluctuation from reducing the frequency to one-third and below. Hence, a reduced sampling frequency does not explain the mass decrease. Ice dynamics that affected the transect occurred from 11 and 12 March 2020 and thereafter. Hence, no ice dynamics influenced the sampling on 5 March 2020. Nevertheless, an impact on the time series cannot be excluded from 12 March 2020 on. Looking at horizontal mass flux and decreased computed snow mass together, we cannot say for sure that erosion was largely responsible for the mass decrease between 27 February and 5 March. The threshold friction velocity was still exceeded on 27 February, indicating snow transport, while low recorded mass flux indicates low transport. The computed threshold friction velocity after Bagnold (1941) (Fig. 11e) does not indicate much more

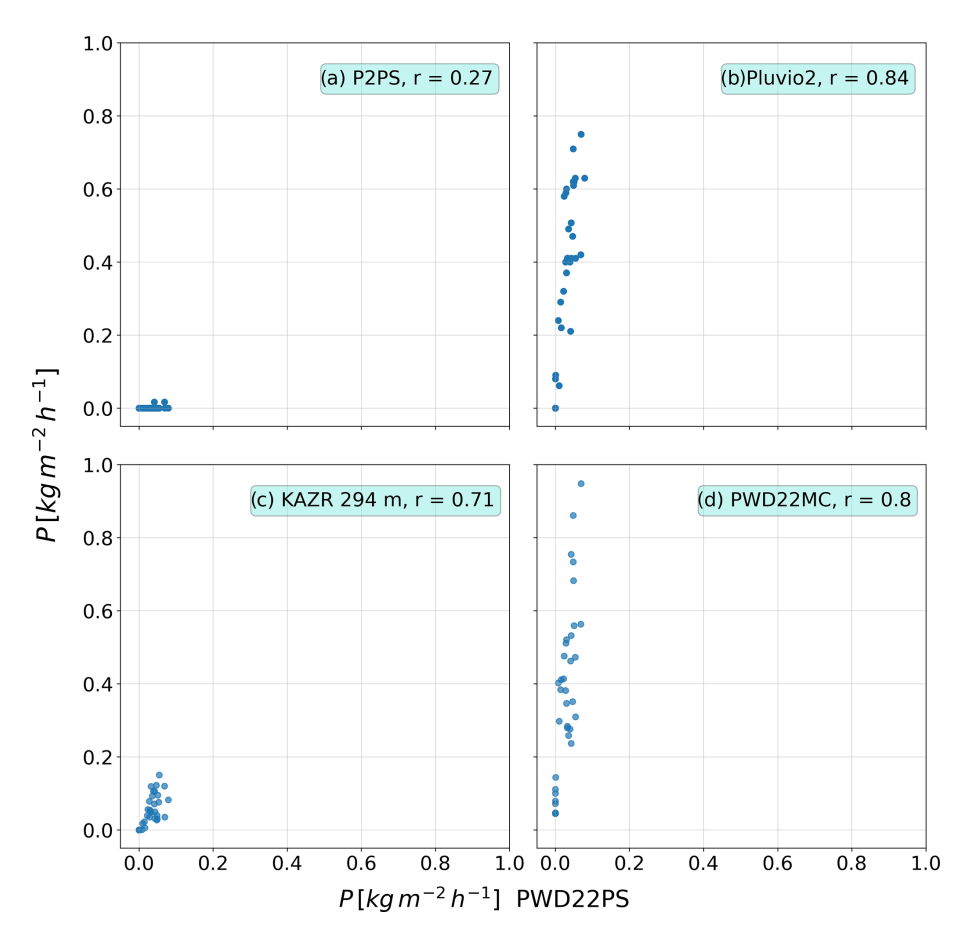


Figure 13. Scatter plots of PWD22PS snowfall rates vs. different sensor snowfall rates for the drifting snow event on 24–25 February 2020 for (a) P2PS, (b) Pluvio2, (c) KAZR and (d) PWD22MC.

or less drifting snow compared to other time periods. However, the formula after Bagnold (1941) is rather simple and neglects varying temperatures and therefore varying bond strengths of snow particles at the top of the snowpack. The bond strength depends strongly on weather history. The preceding long period of air and snow surface temperatures often below -30 °C (Fig. 11c) could have inhibited sintering, which is strongly temperature-dependent and develops more slowly at lower snow temperatures (Colbeck, 1997, 1998; Blackford, 2007). The Bagnold formula does not consider splash entrainment (Comola et al., 2017; Comola and Lehning, 2017) or surface roughness and atmospheric stability, which largely affects the near-surface wind field. Furthermore, the used bond strength parameter of A = 0.18 we used in Eq. (9) was found by Clifton et al. (2006) in a wind tunnel, with an ambient temperature range of -16 to 0 °C. However, this temperature range was undershot most of the time during our investigation period of MOSAiC (Fig. 11c).

In any case, we expect the transect time series until and including 5 March 2020 to be mostly valid. However, the usage of the transect SWE for sensor and reanalysis comparisons is limited, as erosion has very likely occurred over

some periods between the transect sampling days. Hence, the amount of erosion is not quantifiable based on the available transect data. Nonetheless, days where it is likely that no erosion occurred since the previous transect sampling prior to 20 February 2020 could be detected by means of snow particle counters. The cumulative transect SWE of these time periods was then compared against cumulative SWE from the sensors and ERA5 for the same time periods, which will be discussed in the next section. The validity of the SWE time series decreased with increasing ice dynamics from 11 and 12 March 2020 on and with decreasing temporal sampling frequency on both the northern and southern transect loops.

If we assume, based on the findings, that PWD22PS is least affected by blowing snow and provides a reasonable estimate of snowfall, then the snowfall between 31 October 2019 and 26 April 2020 was about 72 mm. We know that the PWD22PS showed the lowest cumulative snowfall and a systematic negative bias compared against ground truth (Fig. 12). Further, it has been suggested that PWD22PS tends to underestimate snowfall, with values of down to 30 % less compared to a Geonor gauge within a DFIR (Wong (2012), Table 1). Until 7 May 2020 as the end of MOSAiC leg 3,

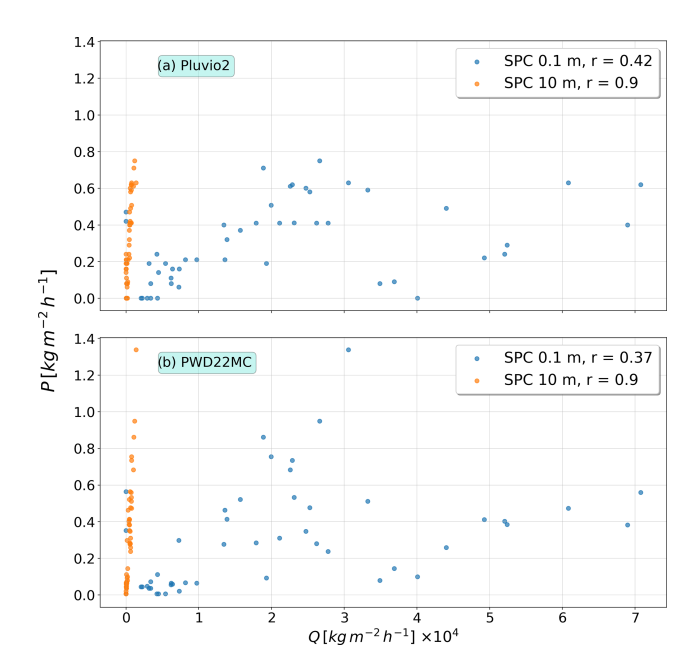


Figure 14. Scatter plots of sensor snowfall rates (y axis) vs. SPC mass flux (x axis) for the drifting snow event on 24–25 February 2020 for (a) Pluvio2 and (b) PWD22MC.

the total snowfall would then be at least about 98 mm in 189 d. If we assume the estimated snowfall from the KAZR to be the upper limit for cumulative snowfall (as it was demonstrated that Pluvio2 and PWD22MC were affected by wind and blowing snow towards overestimation), we find about 114 mm. This value is comparable with the cumulative snowfall from ERA5 (110 mm). Hence, on 189 d, we have as the best estimate that the total snowfall was between 98 and 114 mm. With the total mass increase of 38 mm for the transect SWE during the full observation time, we can approximately compute the minimum total eroded mass as 34 mm until 26 April 2020. With almost 50 % of eroded snow mass, we find magnitudes comparable to those of Leonard and Maksym (2011), although they investigated snow over Antarctic sea ice and their time period for investigation was only about 1 month. However, our findings also compare well to results from Essery et al. (1999). Further sensor assessment discussions are made in the next section.

Sublimation of snow crystals during trace precipitation or diamond dust could have led to snowfall detection in the optical sensors but no SWE increase in the snow cover. However, the study design does not currently allow investigation, but it is recommended to investigate in detail. Earlier studies suggest that blowing snow sublimation may be responsible for about 6% for the mass sink (Chung et al., 2011). The relatively low sublimation rates also arise from the high relative humidities found over sea ice, inhibiting further sublimation due to a quick saturation of the air. Snow cover sublimation can generally be expected to be negligible during polar night (Webster et al., 2021).

Studies of Déry and Tremblay (2004), Leonard et al. (2008), and Leonard and Maksym (2011) indicate that, besides sublimation, large parts of drifting and blowing snow will drift into the open water of leads. However, for the drifting snow event on 24–25 February, there was no significant open water area in the vicinity. Thus, without such a local sink, we would expect that even though snow was eroded, more snow mass would be delivered from the upwind side at approximately the same amount. However, the given mass of drifting snow from the upwind side depends on the lowpressure system's extent and trajectory associated with the high wind speeds. In Fig. 11 we see that after the event, some atmospheric parameters have changed significantly and rapidly (a temperature drop, a decrease in wind speed). The rapid change of atmospheric conditions could explain why no "new" snow has been transported from the windward side. Another important factor could be that the area the transect covers has a relatively low surface roughness, with ridges that were generally shorter than in the surrounding region. Erosion might be large over these relatively smooth areas that the transect covers, and the delivered drifting snow from the upwind side could have been deposited at higher ridges upwind. But even a just frozen lead will be filled by drifting snow after a while, which would lead to a mass sink on the upwind side, inhibiting further snow transport downwind. Considering the ALS-based digital elevation map of the floe (Fig. 2) and the wind direction around 24-25 February (between north and north-east) (Fig. 11b), it is evident that the northern transect was likely to be partially wind-shadowed by higher surface structures on the upwind side. This wind shadowing can lead to less wind transport downwind but maybe also to less erosion due to lower surface friction. This is suggested by our findings, too, as we found more substantial erosion over the northern transect loop. During the drifting snow event, the southern transect was often in the wind shadow of the vessel and other installations (Fig. 2), leading to deceleration and less surface friction that could have led to snow transport or erosion. In the case of more deposition upwind, the mass over the sampled area would decrease even if the friction velocity behind the obstacles is decreased, which leads to less erosion. The computed SWE would not be representative for the whole floe in this case. While potentially interesting, the method used in our study does not allow the investigation of these balances. Another reason for a computed SWE decrease during the later part of the observations might be wind-induced compaction of the upper snowpack. With our approach, we assume almost a linear relationship between snow depth and SWE. However, snowdrifts consist of densely packed, rounded grains (Fierz et al., 2009). Hence, in this case, we probably under-estimate the increase (decrease) of the SWE in the case of drifting snow deposition (erosion). A thorough investigation is recommended but beyond the scope of this study. Further studies based on SMP measurements are planned. Another reason for underestimating snow depth with spatio-temporal sampling ap-

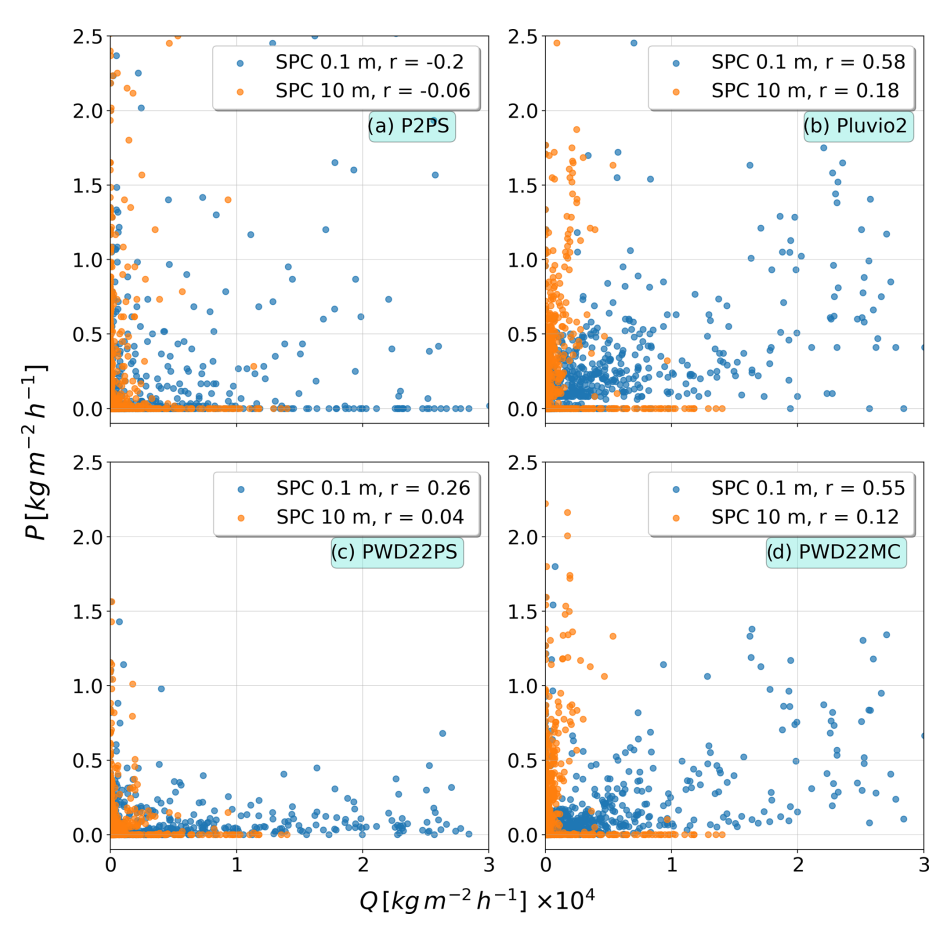


Figure 15. Scatter plots of sensor-computed snowfall rates (y axes) vs. SPC mass flux (x axes) for the whole time period for (a) P2PS, (b) Pluvio2, (c) PWD22PS and (d) PWD22MC.

proaches might be that parts of the snow are caught in the porous parts of ridges, depending on wind direction and on the age of the ridges. This is something that is not covered by this study. Furthermore, for the erosion, the upper snow-pack's microstructural composition plays a role, especially the strength of the bonds associated with sintering and temperature.

4.2 Snowfall sensor estimates

Snowfall rates from precipitation gauges show large differences among each other. Battaglia et al. (2010) already showed that OTT Parsivel instruments overestimate the number of large particles. Further, the uncertainty they found regarding fall velocity was high. Wong (2012) also found a large overestimation of snowfall for the OTT Parsivel of about 50 % (Table 1), while the overestimation became larger during high wind speeds. The relatively low accuracy of $\pm\,20\,\%$ for snowfall as given by the manufacturer compared to other instruments does make strong overestimations not surprising. Observations examined here appear to confirm this overestimation. Although the installation on the top deck

of RV *Polarstern* at 24 m height appears to be well protected against blowing snow (Fig. 15a), the overestimation of P2PS rather appears to be due to wind itself as also found in earlier studies.

Regarding Vaisala PWD22 and snowfall, Boudala et al. (2016) found that in comparison with manual measurements, it overestimated snowfall by about 33 % due to detected snow crystals not observed by the human observer. Wong et al. (2012) instead found good agreements with two Vaisala VRG 101 (double-alter shielded) and two OTT Pluvio (Tretyakov shielded) gauges. Compared to a Geonor gauge in a double fence intercomparison reference (DFIR), Wong (2012) found an underestimation for solid precipitation of 32 % for the PWD22. Hence, we expect and also can confirm an underestimation of snowfall during MOSAiC. However, with 1.1 mm the RMSE was the lowest compared against all other validated sensors. Wong (2012) found little wind influence on the PWD22 measurements, which we can confirm, as the RMSE relative to SWE estimates was reduced least (as relative value) compared against all other sensors after drifting snow periods were eliminated from the comparison. Compared against SPC mass flux, we demonstrated that the installation on the railing on the top deck of RV *Polarstern* has protected the sensor from blowing snow. Conversely, the same device installed in met city on the ice showed a relative overestimate, suggesting an influence from blowing snow. Comparisons with the KAZR-derived snowfall, which is also unaffected by blowing snow, further support the notion that the PWD22PS was not significantly impacted by blowing snow.

The undercatch of snowfall due to the wind for weighing bucket gauges is well known (Goodison et al., 1998; Boudala et al., 2016; Kochendorfer et al., 2017). However, we observed a strong positive bias in the cumulative snow mass for the Pluvio2 gauge when comparing with PWD22PS. This bias was largely due to a strong drifting snow event at the end of February, probably leading to blowing snow being lifted from the ground and landing in the bucket (Figs. 14, 15). Available transfer functions (e.g. Goodison et al., 1998; Boudala et al., 2016; Kochendorfer et al., 2017, 2018) cannot correct for this type of blowing snow event, as they correct the underestimation with increasing wind speed. However, we suggest that these events can be detected using snow particle counters and removed before applying other corrections.

The snowfall retrieval from the KAZR using a Z_e -S relationship with coefficients determined by Matrosov (2007) shows an overestimation relative to the snow cover SWE but performs comparably as well as ERA5. The difference to ERA5 in cumulative snowfall was only about 5 mm by the end of the investigation period. Considering the known low bias in PWD22 measurements, and the fact that the radar snowfall retrievals are not affected by wind or blowing snow, it is likely that this radar-based estimate provides reasonable results. However, such radar-based retrievals are dependent on the inherent properties of the snowfall observed in the datasets from which they are derived.

4.3 ERA5 performance

ERA5 performed reasonably well, with a weak overestimation when compared with snow cover SWE. Overall, the timing of the snowfall events is represented well by ERA5. Relative to PWD22PS, the cumulative ERA5 snowfall would have been overestimated by about 25 % by 7 May 2020. However, as already discussed, due to the light underestimation of the PWD22PS, the true snowfall probably lies between PWD22PS and ERA5 or the KAZR. Relative to PWD22PS, ERA5 appears to perform better before about March 2020, although the available data do not allow us to prove that it generally performs worse before. As the ERA5 performance depends on input of measurements and numerical weather data, we can at least point out that there was a substantial decrease in the air-based (minus 50 %-75 % between March and May 2020; Chen, 2020) and ship-based observations, which may lead to a worsening of the performance. Chen (2020) found a worsening of temperature forecasts of up to 2°C globally in the time period March-May 2020, compared against February 2020. Nonetheless, a comparison with the cumulative sum of the KAZR (Fig. 10b) rather speaks against this theory as the ERA5 cumulative snowfall is always below the KAZR snowfall. Exact reasons with respect to ERA5 should be thoroughly investigated. Cabaj et al. (2020) also found a general positive bias (in daily snowfall rates) comparing ERA5 with CloudSat data. However, CloudSat is only available up to 82° N, while MOSAiC was north of 84° N most of the time and for large parts even above 87° N (Fig. 1) between October 2019 and May 2020. Further, in Cabaj et al. (2020), they found a decrease in the positive bias towards the spring months compared with the winter months of December, January and February while we find an increased apparent bias during this time when comparing with PWD22PS. Wang et al. (2019a) compared ERA5 snowfall with data from several snow buoys for a drift track in the Arctic Ocean comparable to that of MOSAiC and a time span comparable to that of our validation, from autumn to spring in the following year. Although they do not give details about the method, they mention a positive bias of ERA5 cumulative snowfall of about 63 mm compared with snow buoys by the end of the investigation period. They partially found a negative bias and very varying results but on average a positive bias. However, as already pointed out, a conclusion cannot be drawn from a few point measurements on the overall accumulated snow on a larger area. Further, from our study we see that we cannot draw a conclusion from the computed SWE of the snow cover alone on the precipitated sum as the erosion appears to be large, even when measured over larger areas. Nonetheless, the results from Wang et al. (2019a) also indicate that a lot of snow mass gets eroded over time, which is even more evident as we as well as Cabaj et al. (2020) find an overestimation tendency for ERA5 snowfall. We must further notice that ERA5 does not consider blowing snow sublimation in their computations. Although Orsolini et al. (2019) do not find a mass effect of including blowing snow sublimation in ERA5, Chung et al. (2011) for instance computed a larger effect of blowing snow sublimation of $12 \,\mathrm{mm}\,\mathrm{yr}^{-1}$ over sea ice over $324 \,\mathrm{d}$. The non-existent blowing snow particle sublimation may be a reason for the overestimation tendency found in our study. Recent results with a new model of drifting snow sublimation (CRYOWRF; Sharma et al., 2021) indicate that it may be more important than previously estimated. We plan to address this particular problem in our future work.

5 Conclusions

We fitted a snow depth–SWE function to computed SWE values from SnowMicroPen force signals and applied the model to snow depths from Magnaprobes for the northern and southern transect loops of MOSAiC, for the winter and spring periods between October 2019 and May 2020. We show that the SWE reconstructions compared well against direct SWE measurements. Besides transect paths, other snow

depth sources, such as snow height differences from terrestrial laser scans, could be used with this function to compute SWE.

One particular finding of our work is that SWE differences between snow on deformed SYI and snow on remnant SYI and FYI decrease until the end of the snow accumulation season at the beginning of May. The SWE on remnant SYI and FYI, while starting out at only about 50% in late October 2019, reached almost 90 % of the value for snow on deformed SYI by the end of April. Since SWE also did not increase much after 20 February, the observations raise the question as to whether there is a saturation point for snow mass accumulation. We suggest a range of 34 mm (47 %) to 69 mm (68 %) of precipitation that has been eroded over time, with the PWD22PS as a lower limit and the KAZR as an upper limit of cumulative snowfall. There was a remarkable snow erosion event between 24 and 25 February 2020, which we decided to have a closer look into as snow cover SWE decreased during this time. The fate of the eroded snow is unclear, but it is likely that a significant amount was deposited around higher ridges or filled in the gaps of frozen leads, limiting its transport to the areas covered by the transects. However, as transects were conducted approximately weekly, processes in the snow that have occurred in the meantime are not detected. More snow erosion accompanies the temporal adjustment of the surface roughness between remnant SYI and deformed SYI. Besides temporal sampling frequency of the transect, another limitation of the study is that layering of the snowpack was not considered for estimating deposited and eroded snow mass. However, validation measurements at different points in time suggest that the impact of this effect might be small. A thorough investigation of layer density is recommended. Further research, connecting snow microstructure with snow transport rates, for instance, investigating sintering and bond strengths of snow grains that depend on temperature, could help to elucidate high Arctic snow processes. This is also important as the eroded snow has influenced several sensors' measurements.

Although the unquantified eroded snow mass limits the potential for inter-comparisons, we found that the Vaisala Present Weather Detector 22 optical precipitation sensor installed on Polarstern showed the smallest differences with the estimated SWE during periods without indication of drifting snow. We demonstrated that this PWD22 was mostly protected from blowing snow influences while this blowing snow led to high correlations between horizontal mass flux and precipitation rates of the pluviometer and the present weather detector at met city. We assume that the high snowfall rates detected with the ice-based pluviometer originate significantly from blowing snow that was blown into the gauge opening. Similar to PWD22 on Polarstern, the KAZR snowfall retrievals are likely not affected by wind or blowing snow. The snowfall retrieved with this K_a -band radar shows a relatively high bias relative to the snow cover SWE, and it appears to overestimate snowfall. This overestimation however can be reduced when doing more research on selecting range gates and fitting of the coefficients. The OTT Parsivel² laser disdrometer showed a strong tendency towards overestimation. For the Vaisala Present Weather Detector 22, installed on *Polarstern*, we find a total cumulative snowfall of 98 mm over 189 d. We suggest the KAZR snowfall as a possible upper cumulative limit of 114 mm. Snowfall rates from the ERA5 reanalysis showed a reasonable performance, with a good timing of snowfall events but a relatively safe tendency towards overestimation. This light overestimation may arise from non-existing blowing snow sublimation. However, to our knowledge, we present the first validation of ERA5 snowfall for the high Arctic, based on a combination of repeating snow depth transects and a set of in situ precipitation sensor data.

This study sets the base for future snow mass balance research for MOSAiC and further general snow research for Arctic sea ice. We are better aware of snow mass quantities that accumulate and erode over the central Arctic sea ice surface for almost the whole accumulation season, including the polar night. The data can be used to improve numerical snow cover, sea ice, and weather and climate models and for more detailed process-understanding research across disciplines. Initial sensor validations were conducted, which allow for more specified, more thorough research.

Appendix A: SWE comparison with Sturm et al. (2002a)

We can compare the HS-SWE function (SWE = $323.97 \cdot \mathrm{HS^{1.07}}$, with HS in metres) with the fitted function from Sturm et al. (2002a) (SWE = $0.348 \cdot \mathrm{HS}$, with HS in centimetres), derived for sea ice snow cover during the SHEBA campaign (Perovich et al., 1999; Uttal et al., 2002). It is shown that the fit in this paper (hereby called "W2021") generally delivers lower SWE values for the same snow height compared against Sturm et al. (2002a) (hereby called "S2002"). The difference becomes larger the higher the snow depth is, which is partially a result of the different gradient (323.97 vs. 348). However, there is also a faster change between 0 and 200 mm, which is a result of the slight non-linearity of the W2021 function. The overall difference is significant, as the deviation of the overall average from S2002 (86.5 mm) to W2021 (74 mm) is +17%, while the RMSE is 13 mm.

This deviation is relevant, especially when comparing ground truth with snowfall sensors in such a dry environment as the Arctic, where average yearly snowfall rates are typically very small. These points justify the application of a specific fit for the winter and early spring during MOSAiC, instead of using values from literature. Differences in comparison with Sturm et al. (2002a) stand out very quickly. They found an average snow depth of 0.337 m and an average density of 340 kg m⁻³ resulting in 166 mm SWE. We found an average snow depth of 0.249 m and an average density of 286.5 kg m⁻³. Hence, both values are lower in our

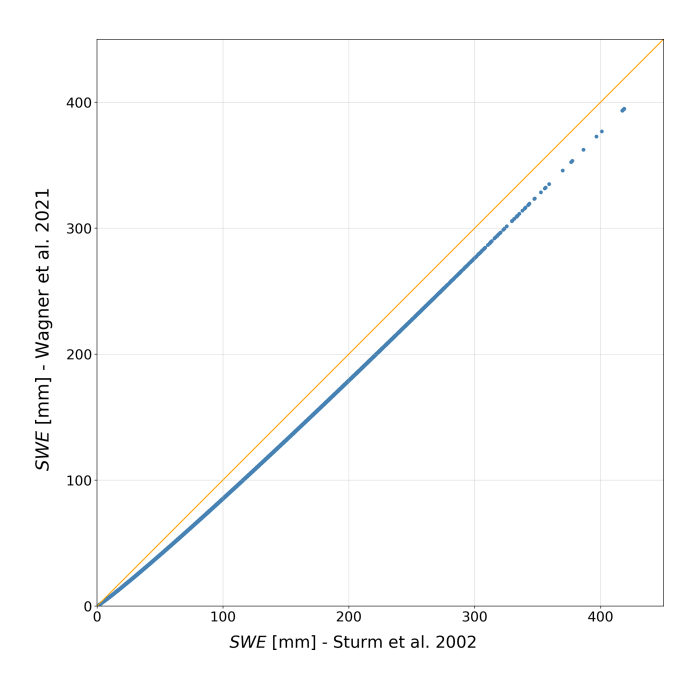


Figure A1. Scatter plot of derived SWE after fitted function in this paper and function by Sturm et al. (2002a). The orange line marks where r = 1.0.

study, resulting in an average SWE of 71.2 mm. This is indeed less than the half found by Sturm et al. (2002a). Note that the timing and setup of the snow measurements of Sturm et al. (2002a) are indeed comparable to ours, as they conducted snow transect measurements along transects for the accumulation period from October to May, as well. However, they used different instrumentation and also sampled over different horizontal extents. As discussed above, the average SWE change due to a snow transport event can be very different when we compare one transect section SWE against the whole transect SWE. Hence, comparability is always subject to great uncertainties. Also note that Sturm et al. (2002a) found a 25 % higher value of snow cover SWE, compared against snowfall measurements with a Nipher shielded gauge, even after applying a 2.5 factor as precipitation correction against undercatch. The lower SWE on the snow cover is in any case very contrary to our results, as we estimate at least 56% less snow mass on the ice compared against measured snowfall. A larger impact on the results could be due to the fact that the measuring during our investigation period did mostly occur between the 85th and 83th latitude, while during SHEBA, the camp started at around 75° N, 142° W and drifted up to 75° N, 162° W. We can speculate that a less dry climate further away from the pole led to more snowfall, or that certain weather patterns led to notable differences over longer time spans in snowfall, wind conditions or temperature, which we cannot determine at this point. Given that fitting the HS-SWE function is highly specific for given snow conditions and considering the substantial different average snow depth and snow density, we conclude that these are the main reasons for different fitting parameters that are found for our study. Nonetheless, the measuring setup and instrumentation itself might lead to differences and cannot be easily quantitatively compared.

Data availability. KAZR (https://doi.org/10.5439/1498936; Lindenmaier et al., 2019), PWD22 (https://adc.arm.gov/discovery/#/ results/instrument_code::pwd, last access: 14 June 2022; Kyrouac and Holdridge, 2019), Parsivel² (https://doi.org/10.5439/1498731; Shi, 2019) and Pluvio² data (https://adc.arm.gov/discovery/#/ results/datastream::moswbpluvio2S3.a1, last access: 14 June 2022 Wang et al., 2019b) are publicly available in the ARM data archive. The following data sets will be publicly accessible by 1 January 2023 on the PANGAEA data publisher. Derived SWE from the SnowMicroPen is available at https://doi.pangaea. de/10.1594/PANGAEA.92746 (Wagner et al., 2021). Raw SMP data are available at https://doi.org/10.1594/PANGAEA.935554 (Macfarlane et al., 2021). Bulk SWE measurements are available at https://doi.org/10.1594/PANGAEA.940199 (Macfarlane et al., 2022). Magnaprobe snow depths are available at https://doi.org/10.1594/PANGAEA.937781 (Itkin et al., 2021). Raw met tower data are available at the Arctic Data Center (https://doi.org/10.18739/A2VM42Z5F; Cox et al., 2021). Data will be available at the UK Polar Data Centre by 15 July 2022 (https: //www.bas.ac.uk/data/uk-pdc/).

Author contributions. DNW took the lead in writing the manuscript and implemented comments, improvements and findings from discussions with co-authors. DNW, JR, NK, ES, MO, IR, MS, MJ, DK, ARM and SA conducted the snow pit measurements. DNW and ARM processed the snow pit data. The principal investigator for snow pits is MS. SH, MO, PI, MJ, SA, JS and RR conducted transect measurements. The principal investigator for the transect is PI. Transect data were post-processed by DNW. MDS, OGP, TU, MMF, AK and CC were responsible for the met tower measurements, including SPC. The principal investigator for the tower is MDS. The University of Colorado/NOAA flux team processed the met tower data. The principal investigator for the SPC is MMF. DNW and MMF post-processed the SPC data. Team ICE created floe maps during the cruise. SH provided the code to correct the coordinate transformation from global to FloeNavi coordinates. The KAZR and all precipitation sensors were set up, maintained and processed by the ARM team, and MDS was the principal investigator for the ARM involvement in MOSAiC. DNW conducted further KAZR and gauge processing. MN led the ice team during MOSAiC and coordinated the work of the different sub-groups within the ice team. ML was involved in MOSAiC planning and supervised the work during the manuscript preparation.

Competing interests. The contact author has declared that neither they nor their co-authors have any competing interests.

Disclaimer. Publisher's note: Copernicus Publications remains neutral with regard to jurisdictional claims in published maps and institutional affiliations.

Acknowledgements. Data used in this paper were produced as part of the international Multidisciplinary drifting Observatory for the Study of the Arctic Climate (MOSAiC) with the tag MOSAIC20192020 and the project ID: AWI_PS122_00. KAZR reflectivities and precipitation data were obtained from the Atmospheric Radiation Measurement (ARM) user facility, a U.S. Department of Energy (DOE) Office of Science user facility managed by the Biological and Environmental Research Program. We thank Sergey Matrosov for valuable discussions about snowfall and for helping with his radar expertise. The authors thank all MOSAiC participants for contributing to the paper in one way or another: the MOSAiC logistics team, the ship's personnel, all the different team members (ICE, ATMOS, BGC, ECO, OCEAN), the ARM crew, the project coordination and the MOSAiC project board. We also refer to the extended acknowledgement for MOSAiC (Nixdorf et al., 2021).

Financial support. David N. Wagner and Michael Lehning were supported by the Swiss National Science Foundation (grant no. SNSF-200020_179130). Martin Schneebeli, Amy R. Macfarlane and David N. Wagner were supported by the Swiss Polar Institute (grant no. DIRCR-2018-003). Martin Schneebeli and Amy R. Macfarlane were supported by the European Union's Horizon 2020 research and innovation program projects ARICE (grant no. 730965) for berth fees associated with the participation of the DEARice project and the WSL Institute for Snow and Avalanche Research SLF (grant no. WSL_201812N1678). Met tower data were supported by the National Science Foundation (grant no. OPP-1724551) and by NOAA's Physical Sciences Laboratory (PSL) and Global Ocean Monitoring and Observing Program (GOMO). Matthew D. Shupe was supported by the DOE Atmospheric System Research Program (grant nos. DE-SC0019251 and DE-SC0021341). Polona Itkin was supported by the National Science Foundation (grant no. NSF-1820927) and by the Research Council of Norway (grant no. RCN-287871). Stefanie Arndt, Stefan Hendricks, Daniela Krampe, Marcel Nicolaus, Robert Ricker and Julia Regnery were supported through the Alfred Wegener Institute funds AWI_SNOW, AWI_ICE and AWI_ROV. Stefanie Arndt and Marcel Nicolaus were supported through the German Research Foundation (DFG) projects SnowCast (grant no. AR1236/1) and SCASI (grant no. NI1095/5).

Review statement. This paper was edited by Michel Tsamados and reviewed by Joshua King and one anonymous referee.

References

Alfred-Wegener-Institut Helmholtz-Zentrum für Polar und Meeresforschung: Polar Research and Supply Vessel POLARSTERN Operated by the Alfred-Wegener-Institute, Journal of large-scale research facilities, 3, A119, https://doi.org/10.17815/jlsrf-3-1631, 2017.

- Bagnold, R. A. (Ed.): The physics of blown sand and desert dunes, Methuen & Co., London, 1941.
- Bartholomew, M.: Weighing Bucket Rain Gauge Instrument Handbook., Tech. rep., edited by: Stafford, R., ARM user facility. DOE/SC-ARM-TR-232, 2020a.
- Bartholomew, M.: Laser Disdrometer Instrument Handbook., Tech. rep., edited by: Stafford, R., ARM user facility, DOE/SC-ARM-TR-137, 2020b.
- Batrak, Y. and Müller, M.: On the warm bias in atmospheric reanalyses induced by the missing snow over Arctic sea-ice, Nat. Commun., 10, 1–8, https://doi.org/10.1038/s41467-019-11975-3, 2019.
- Battaglia, A., Rustemeier, E., Tokay, A., Blahak, U., and Simmer, C.: PARSIVEL Snow Observations: A Critical Assessment, J. Atmos. Ocean. Tech., 27, 333–344, https://doi.org/10.1175/2009JTECHA1332.1, 2010.
- Blackford, J. R.: Sintering and microstructure of ice: a review, J. Phys. D, 40, R355–R385, https://doi.org/10.1088/0022-3727/40/21/r02, 2007.
- Boudala, F. S., Isaac, G. A., Filman, P., Crawford, R., Hudak, D., and Anderson, M.: Performance of emerging technologies for Measuring Solid and Liquid Precipitation in Cold Climate as compared to the Traditional Manual Gauges, J. Atmos. Ocean. Tech., 34, 167–185, https://doi.org/10.1175/jtech-d-16-0088.1, 2016.
- Budd, W. F., Dingle, W. R. J., and Radok, U.: The Byrd Snow Drift Project: Outline and Basic Results, American Geophysical Union (AGU), 71–134, https://doi.org/10.1029/AR009p0071, 1966.
- Cabaj, A., Kushner, P. J., Fletcher, C. G., Howell, S., and Petty, A. A.: Constraining Reanalysis Snowfall Over the Arctic Ocean Using CloudSat Observations, Geophys. Res. Lett., 47, 4, https://doi.org/10.1029/2019gl086426, 2020.
- Calonne, N., Richter, B., Löwe, H., Cetti, C., ter Schure, J., Van Herwijnen, A., Fierz, C., Jaggi, M., and Schneebeli, M.: The RHOSSA campaign: multi-resolution monitoring of the seasonal evolution of the structure and mechanical stability of an alpine snowpack, The Cryosphere, 14, 1829–1848, https://doi.org/10.5194/tc-14-1829-2020, 2020.
- Chen, Y.: COVID-19 Pandemic Imperils Weather Forecast, Geophys. Res. Lett., 47, e2020GL088613, https://doi.org/10.1029/2020gl088613, 2020.
- Chung, Y.-C., Bélair, S., and Mailhot, J.: Blowing Snow on Arctic Sea Ice: Results from an Improved Sea Ice–Snow–Blowing Snow Coupled System, J. Hydrometeorol., 12, 678–689, https://doi.org/10.1175/2011JHM1293.1, 2011.
- Clifton, A., Rüedi, J.-D., and Lehning, M.: Snow saltation threshold measurements in a drifting-snow wind tunnel, J. Glaciol., 52, 585–596, https://doi.org/10.3189/172756506781828430, 2006.
- Colbeck, S.: Sintering in a dry snow cover, J. Appl. Phys., 84, 4585–4589, https://doi.org/10.1063/1.368684, 1998.
- Colbeck, S. C.: A Review of Sintering in Seasonal Snow Cover, CRREL Report 97–10, 11 pp., 1997.
- Comola, F. and Lehning, M.: Energy- and momentum-conserving model of splash entrainment in sand and snow saltation, Geophys. Res. Lett., 44, 1601–1609, https://doi.org/10.1002/2016GL071822, 2017.
- Comola, F., Kok, J. F., Gaume, J., Paterna, E., and Lehning, M.: Fragmentation of wind-blown snow crystals, Geophys. Res.

- Lett., 44, 4195–4203, https://doi.org/10.1002/2017GL073039, 2017
- Cox, C., Gallagher, M., Shupe, M., Persson, O., Solomon, A., Blomquist, B., Brooks, I., Costa, D., Gottas, D., Hutchings, J., Osborn, J., Morris, S., Preusser, A., and Uttal, T.: 10-meter (m) meteorological flux tower measurements (Level 1 Raw), multi-disciplinary Drifting Observatory for the Study of Arctic Climate (MOSAiC), central Arctic, October 2019–September 2020 [data set], https://doi.org/10.18739/A2VM42Z5F, 2021.
- Déry, S. J. and Tremblay, L.-B.: Modeling the Effects of Wind Redistribution on the Snow Mass Budget of Polar Sea Ice, J. Phys. Oceanogr., 34, 258–271, https://doi.org/10.1175/1520-0485(2004)034<0258:MTEOWR>2.0.CO;2, 2004.
- Déry, S. J. and Yau, M. K.: A climatology of adverse winter-type weather events, J. Geophys. Res.-Atmos., 104, 16657–16672, https://doi.org/10.1029/1999jd900158, 1999.
- Déry, S. J. and Yau, M. K.: Large-scale mass balance effects of blowing snow and surface sublimation, J. Geophys. Res.-Atmos., 107, ACL 8-1–ACL 8-17, https://doi.org/10.1029/2001jd001251, 2002.
- Déry, S. J., Taylor, P. A., and Xiao, J.: The Thermodynamic Effects of Sublimating, Blowing Snow in the Atmospheric Boundary Layer, Bound.-Lay. Meteorol., 89, 251–283, https://doi.org/10.1023/a:1001712111718, 1998.
- Essery, R., Li, L., and Pomeroy, J.: A distributed model of blowing snow over complex terrain, Hydrol. Process., 13, 2423–2438, https://doi.org/10.1002/(sici)1099-1085(199910)13:14/15<2423::aid-hyp853>3.0.co;2-u, 1999.
- Fierz, C., Armstrong, R. L., Durand, Y., Etchevers, P., Greene, E., McClung, D. M., Nishimura, K., Satyawali, P. K., and Sokratov, S. A.: The International Classification for Seasonal Snow on the Ground. IHP-VII Technical Documents in Hydrology No. 83, IACS Contribution No. 1, UNESCO-IHP, Paris, 2009.
- Filhol, S. and Sturm, M.: Snow bedforms: A review, new data, and a formation model, J. Geophys. Res.-Earth Surf., 120, 1645–1669, https://doi.org/10.1002/2015JF003529, 2015.
- Goodison, B., Louie, P., and Yang, D.: The WMO solid precipitation measurement intercomparison, WMO/TD No. 872, World Meteorological Organization Publications, Geneva, 1998.
- Haberkorn, A. (Ed.): European Snow Booklet, 363 pp., https://doi.org/10.16904/envidat, 59, 2019.
- Hersbach, H., Bell, B., Berrisford, P., Hirahara, S., Horányi, A., Muñoz-Sabater, J., Nicolas, J., Peubey, C., Radu, R., Schepers, D., Simmons, A., Soci, C., Abdalla, S., Abellan, X., Balsamo, G., Bechtold, P., Biavati, G., Bidlot, J., Bonavita, M., De Chiara, G., Dahlgren, P., Dee, D., Diamantakis, M., Dragani, R., Flemming, J., Forbes, R., Fuentes, M., Geer, A., Haimberger, L., Healy, S., Hogan, R. J., Hólm, E., Janisková, M., Keeley, S., Laloyaux, P., Lopez, P., Lupu, C., Radnoti, G., de Rosnay, P., Rozum, I., Vamborg, F., Villaume, S., and Thépaut, J.-N.: The ERA5 global reanalysis, Q. J. Roy. Meteor. Soc., 146, 1999–2049, https://doi.org/10.1002/qj.3803, 2020.
- Holtsmark, B. E.: Insulating Effect of a Snow Cover on the Growth of Young Sea Ice, Arctic, 8, 60–65, 1955.
- Iacozza, J. and Barber, D. G.: An examination of the distribution of snow on sea-ice, Atmosphere-Ocean, 37, 21–51, https://doi.org/10.1080/07055900.1999.9649620, 1999.

- IFS Documentation CY47R1 Part IV: Physical Processes, no. 4 in IFS Documentation, ECMWF, https://doi.org/10.21957/cpmkqvhja, 2020.
- Itkin, P., Webster, M., Hendricks, S., Oggier, M., Jaggi, M., Ricker, R., Arndt, S., Divine, D. V., von Albedyll, L., Raphael, I., Rohde, J., and Liston, G. E.: Magnaprobe snow and melt pond depth measurements from the 2019-2020 MOSAiC expedition, PANGAEA [data set], https://doi.org/10.1594/PANGAEA.937781, PANGAEA, 2021.
- Jonas, T., Marty, C., and Magnusson, J.: Estimating the snow water equivalent from snow depth measurements in the Swiss Alps, J. Hydrol., 378, 161–167, https://doi.org/10.1016/j.jhydrol.2009.09.021, 2009.
- Jun, S.-Y., Ho, C.-H., Jeong, J.-H., Choi, Y.-S., and Kim, B.-M.: Recent changes in winter Arctic clouds and their relationships with sea ice and atmospheric conditions, Tellus A, 68, 29130, https://doi.org/10.3402/tellusa.v68.29130, 2016.
- Jutras, M., Vancoppenolle, M., Lourenço, A., Vivier, F., Carnat, G., Madec, G., Rousset, C., and Tison, J.-L.: Thermodynamics of slush and snow-ice formation in the Antarctic sea-ice zone, Deep-Sea Res. Pt. II, 131, 75–83, https://doi.org/10.1016/j.dsr2.2016.03.008, 2016.
- King, J., Howell, S., Brady, M., Toose, P., Derksen, C., Haas, C., and Beckers, J.: Local-scale variability of snow density on Arctic sea ice, The Cryosphere, 14, 4323–4339, https://doi.org/10.5194/tc-14-4323-2020, 2020.
- King, J. C., Pomeroy, J. W., Gray, D. M., and Fierz, C.: Snow accumulation, in: Snow and Climate, edited by Armstrong, R. L. and Brun, E., chap. 3.4, 83–92, Cambridge University Press, 2008.
- Kochendorfer, J., Rasmussen, R., Wolff, M., Baker, B., Hall, M. E., Meyers, T., Landolt, S., Jachcik, A., Isaksen, K., Brækkan, R., and Leeper, R.: The quantification and correction of wind-induced precipitation measurement errors, Hydrol. Earth Syst. Sci., 21, 1973–1989, https://doi.org/10.5194/hess-21-1973-2017, 2017.
- Kochendorfer, J., Nitu, R., Wolff, M., Mekis, E., Rasmussen, R., Baker, B., Earle, M. E., Reverdin, A., Wong, K., Smith, C. D., Yang, D., Roulet, Y.-A., Meyers, T., Buisan, S., Isaksen, K., Brækkan, R., Landolt, S., and Jachcik, A.: Testing and development of transfer functions for weighing precipitation gauges in WMO-SPICE, Hydrol. Earth Syst. Sci., 22, 1437–1452, https://doi.org/10.5194/hess-22-1437-2018, 2018.
- Krumpen, T., Birrien, F., Kauker, F., Rackow, T., von Albedyll, L., Angelopoulos, M., Belter, H. J., Bessonov, V., Damm, E., Dethloff, K., Haapala, J., Haas, C., Harris, C., Hendricks, S., Hoelemann, J., Hoppmann, M., Kaleschke, L., Karcher, M., Kolabutin, N., Lei, R., Lenz, J., Morgenstern, A., Nicolaus, M., Nixdorf, U., Petrovsky, T., Rabe, B., Rabenstein, L., Rex, M., Ricker, R., Rohde, J., Shimanchuk, E., Singha, S., Smolyanitsky, V., Sokolov, V., Stanton, T., Timofeeva, A., Tsamados, M., and Watkins, D.: The MOSAiC ice floe: sediment-laden survivor from the Siberian shelf, The Cryosphere, 14, 2173–2187, https://doi.org/10.5194/tc-14-2173-2020, 2020.
- Kyrouac, J. and Holdridge, D.: Surface Meteorological Instrumentation (PWD), atmospheric Radiation Measurement (ARM) user facility [data set], https://adc.arm.gov/discovery/#/results/instrument_code::pwd (last access: 16 June 2022), 2019.

- Lange, M. A. and Eicken, H.: The sea ice thickness distribution in the northwestern Weddell Sea, J. Geophys. Res.-Oceans, 96, 4821–4837, https://doi.org/10.1029/90JC02441, 1991.
- Leonard, K. C. and Maksym, T.: The importance of wind-blown snow redistribution to snow accumulation on Bellingshausen Sea ice, Ann. Glaciol., 52, 271–278, https://doi.org/10.3189/172756411795931651, 2011.
- Leonard, K. C., Tremblay, L., MacAyeal, D. R., and Jacobs, S. S.: Interactions of wind-transported snow with a rift in the Ross Ice Shelf, Antarctica, Geophys. Res. Lett., 35, 5, https://doi.org/10.1029/2007g1033005, 2008.
- Lindenmaier, I., Nelson, D., Isom, B., Hardin, J., Matthews, A., Wendler, T., and Castro, V.: Ka ARM Zenith Radar (KAZR-CFRGE), atmospheric Radiation Measurement (ARM) user facility [data set], https://doi.org/10.5439/1498936, 2019.
- Liston, G. E., Itkin, P., Stroeve, J., Tschudi, M., Stewart, J. S., Pedersen, S. H., Reinking, A. K., and Elder, K.: A Lagrangian Snow-Evolution System for Sea-Ice Applications (SnowModel-LG): Part I Model Description, J. Geophys. Res.-Oceans, 125, e2019JC015913, https://doi.org/10.1029/2019JC015913, 2020.
- Löffler-Mang, M. and Joss, J.: An Optical Disdrometer for Measuring Size and Velocity of Hydrometeors, J. Atmos. Ocean. Tech., 17, 130–139, https://doi.org/10.1175/1520-0426(2000)017<0130:AODFMS>2.0.CO;2, 2000.
- López-Moreno, J. I., Leppänen, L., Luks, B., Holko, L., Picard, G., Sanmiguel-Vallelado, A., Alonso-González, E., Finger, D. C., Arslan, A. N., Gillemot, K., Sensoy, A., Sorman, A., Ertas, M. C., Fassnacht, S. R., Fierz, C., and Marty, C.: Intercomparison of measurements of bulk snow density and water equivalent of snow cover with snow core samplers: Instrumental bias and variability induced by observers, Hydrol. Process., 34, 3120–3133, https://doi.org/10.1002/hyp.13785, 2020.
- Löwe, H. and Herwijnen, A. V.: A Poisson shot noise model for micro-penetration of snow, Cold Reg. Sci. Technol., 70, 62–70, https://doi.org/10.1016/j.coldregions.2011.09.001, 2012.
- Macfarlane, A. R., Schneebeli, M., Dadic, R., Wagner, D. N., Arndt, S., Clemens-Sewall, D., Hämmerle, S., Hannula, H.-R., Jaggi, M., Kolabutin, N., Krampe, D., Lehning, M., Matero, I., Nicolaus, M., Oggier, M., Pirazzini, R., Polashenski, C., Raphael, I., Regnery, J., Shimanchuck, E., Smith, M. M., and Tavri, A.: Snowpit SnowMicroPen (SMP) force profiles collected during the MOSAiC expedition, PANGAEA [data set], https://doi.org/10.1594/PANGAEA.935554, 2021.
- Macfarlane, A. R., Tavri, A., Polashenski, C., Krampe, D., Clemens-Sewall, D., Wagner, D. N., Shimanchuck, E., Hannula, H.-R., Raphael, I., Mateo, I., Regnery, J., Smith, M., Oggier, M., Nicolaus, M., Jaggi, M., Lehning, M., Kolabutin, N., Pirazzini, R., Dadic, R., Hammerle, S., Arndt, S., and Schneebeli, M.: Snowpit metadata during the MOSAiC expedition: SWE, PANGAEA [data set], https://doi.org/10.1594/PANGAEA.940199, 2022.
- Matrosov, S. Y.: Modeling Backscatter Properties of Snowfall at Millimeter Wavelengths, J. Atmos. Sci., 64, 1727–1736, https://doi.org/10.1175/jas3904.1, 2007.
- Matrosov, S. Y., Shupe, M. D., and Djalalova, I. V.: Snowfall Retrievals Using Millimeter-Wavelength Cloud Radars, J. Appl. Meteorol. Climatol., 47, 769–777, https://doi.org/10.1175/2007jamc1768.1, 2008.

- Maykut, G. A. and Untersteiner, N.: Some results from a time-dependent thermodynamic model of sea ice, J. Geophys. Res., 76, 1550–1575, https://doi.org/10.1029/JC076i006p01550, 1971.
- McIlhattan, E. A., Kay, J. E., and L'Ecuyer, T. S.: Arctic Clouds and Precipitation in the Community Earth System Model Version 2, J. Geophys. Res.-Atmos., 125, e2020JD032521, https://doi.org/10.1029/2020jd032521, 2020.
- Merkouriadi, I., Liston, G. E., Graham, R. M., and Granskog, M. A.: Quantifying the Potential for Snow-Ice Formation in the Arctic Ocean, Geophys. Res. Lett., 47, e2019GL085020, https://doi.org/10.1029/2019GL085020, 2020.
- METEK GmbH: Ultrasonic Wind Sensor uSonic-3 Cage MP Datasheet, https://metek.de/wp-content/uploads/2016/09/20161007_Data-sheet_uSonic3_Cage_MP.pdf (last access: 16 June 2022), 2022.
- Nghiem, S. V., Martin, S., Perovich, D. K., Kwok, R., Drucker, R., and Gow, A. J.: A laboratory study of the effect of frost flowers on C band radar backscatter from sea ice, J. Geophys. Res.-Oceans, 102, 3357–3370, https://doi.org/10.1029/96JC03208, 1997.
- Nicolaus, M., Hoppmann, M., Arndt, S., Hendricks, S., Katlein, C., Nicolaus, A., Rossmann, L., Schiller, M., and Schwegmann, S.: Snow Depth and Air Temperature Seasonality on Sea Ice Derived From Snow Buoy Measurements, Front. Marine Sci., 8, 377, https://doi.org/10.3389/fmars.2021.655446, 2021a.
- Nicolaus, M., Perovich, D., Spreen, G., Granskog, M., Albedyll, L., Angelopoulos, M., Anhaus, P., Arndt, S., Belter, H., Bessonov, V., Birnbaum, G., Brauchle, J., Calmer, R., Cardellach, E., Cheng, B., Clemens-Sewall, D., Dadic, R., Damm, E., Boer, G., Demir, O., Dethloff, K., Divine, D., Fong, A., Fons, S., Frey, M., Fuchs, N., Gabarró, C., Gerland, S., Goessling, H., Gradinger, R., Haapala, J., Haas, C., Hamilton, J., Hannula, H.-R., Hendricks, S., Herber, A., Heuzé, C., Hoppmann, M., Høyland, K., Huntemann, M., Hutchings, J., Hwang, B., Itkin, P., Jacobi, H.-W., Jaggi, M., Jutila, A., Kaleschke, L., Katlein, C., Kolabutin, N., Krampe, D., Kristensen, S., Krumpen, T., Kurtz, N., Lampert, A., Lange, B., Lei, R., Light, B., Linhardt, F., Liston, G., Loose, B., Macfarlane, A., Mahmud, M., Matero, I., Maus, S., Morgenstern, A., Naderpour, R., Nandan, V., Niubom, A., Oggier, M., Oppelt, N., Pätzold, F., Perron, C., Petrovsky, T., Pirazzini, R., Polashenski, C., Rabe, B., Raphael, I., Regnery, J., Rex, M., Ricker, R., Riemann-Campe, K., Rinke, A., Rohde, J., Salganik, E., Scharien, R., Schiller, M., Schneebeli, M., Semmling, M., Shimanchuk, E., Shupe, M., Smith, M., Smolyanitsky, V., Sokolov, V., Stanton, T., Stroeve, J., Thielke, L., Timofeeva, A., Tonboe, R., Tavri, A., Tsamados, M., Wagner, D., Watkins, D., Webster, M., and Wendisch, M.: Overview of the MOSAiC expedition -Snow and sea ice, Elementa: Science of the Anthropocene, 10, 000046, https://doi.org/10.1525/elementa.2021.000046, 2021b.
- Nixdorf, U., Dethloff, K., Rex, M., Shupe, M., Sommerfeld, A., Perovich, D., Nicolaus, M., Heuzé, C., Rabe, B., Loose, B., Damm, E., Gradinger, R., Fong, A., Maslowski, W., Rinke, A., Kwok, R., Spreen, G., Wendisch, M., Herber, A., Hirsekorn, M., Mohaupt, V., Frickenhaus, S., Immerz, A., Weiss-Tuider, K., König, B., Mengedoht, D., Regnery, J., Gerchow, P., Ransby, D., Krumpen, T., Morgenstern, A., Haas, C., Kanzow, T., Rack, F. R., Saitzev, V., Sokolov, V., Makarov, A., Schwarze, S., Wunderlich,

- T., Wurr, K., and Boetius, A.: MOSAiC Extended Acknowledgement, Zenodo, https://doi.org/10.5281/zenodo.5179739, 2021.
- Orsolini, Y., Wegmann, M., Dutra, E., Liu, B., Balsamo, G., Yang, K., de Rosnay, P., Zhu, C., Wang, W., Senan, R., and Arduini, G.: Evaluation of snow depth and snow cover over the Tibetan Plateau in global reanalyses using in situ and satellite remote sensing observations, The Cryosphere, 13, 2221–2239, https://doi.org/10.5194/tc-13-2221-2019, 2019.
- Perovich, D. K., Andreas, E. L., Curry, J. A., Eiken, H., Fairall, C. W., Grenfell, T. C., Guest, P., Intrieri, J., Kadko, D., Lindsay, R. W., McPhee, M. G., Morison, J., Moritz, R. E., Paulson, C. A., Pegau, W. S., Persson, P., Pinkel, R., Richter-Menge, J. A., Stanton, T., Stern, H., Sturm, M., Tucker III, W., and Uttal, T.: Year on ice gives climate insights, Eos, Transactions American Geophysical Union, 80, 481–486, https://doi.org/10.1029/EO080i041p00481-01, 1999.
- Petty, A. A., Webster, M., Boisvert, L., and Markus, T.: The NASA Eulerian Snow on Sea Ice Model (NESOSIM) v1.0: initial model development and analysis, Geosci. Model Dev., 11, 4577–4602, https://doi.org/10.5194/gmd-11-4577-2018, 2018.
- Proksch, M., Löwe, H., and Schneebeli, M.: Density, specific surface area, and correlation length of snow measured by high-resolution penetrometry, J. Geophys. Res.-Earth Surf., 120, 346–362, https://doi.org/10.1002/2014JF003266, 2015.
- Sato, T., Kimura, T., Ishimaru, T., and Maruyama, T.: Field test of a new snow-particle counter (SPC) system, Ann. Glaciol., 18, 149–154, https://doi.org/10.3189/S0260305500011411, 1993.
- Savelyev, S. A., Gordon, M., Hanesiak, J., Papakyriakou, T., and Taylor, P. A.: Blowing snow studies in the Canadian Arctic Shelf Exchange Study, 2003–04, Hydrol. Process., 20, 817–827, https://doi.org/10.1002/hyp.6118, 2006.
- Scarchilli, C., Frezzotti, M., Grigioni, P., Silvestri, L. D., Agnoletto, L., and Dolci, S.: Extraordinary blowing snow transport events in East Antarctica, Clim. Dynam., 34, 1195–1206, https://doi.org/10.1007/s00382-009-0601-0, 2009.
- Schneebeli, M. and Johnson, J. B.: A constant-speed penetrometer for high-resolution snow stratigraphy, Ann. Glaciol., 26, 107–111, https://doi.org/10.3189/1998AoG26-1-107-111, 1998.
- Schneebeli, M., Pielmeier, C., and Johnson, J. B.: Measuring snow microstructure and hardness using a high resolution penetrometer, Cold Reg. Sci. Technol., 30, 101–114, https://doi.org/10.1016/S0165-232X(99)00030-0, 1999.
- Serreze, M. C. and Hurst, C. M.: Representation of Mean Arctic Precipitation from NCEP–NCAR and ERA Reanalyses, J. Climate, 13, 182–201, https://doi.org/10.1175/1520-0442(2000)013<0182:romapf>2.0.co;2, 2000.
- Sharma, V., Gerber, F., and Lehning, M.: Introducing CRYOWRF v1.0: Multiscale atmospheric flow simulations with advanced snow cover modelling, Geosci. Model Dev. Discuss. [preprint], https://doi.org/10.5194/gmd-2021-231, in review, 2021.
- Shi, Y.: Laser Disdrometer (LD), atmospheric Radiation Measurement (ARM) user facility [data set], https://doi.org/10.5439/1498731, 2019.
- Shupe, M., Rex, M., Blomquist, B., Persson, P., Schmale, J., Uttal,
 T., Althausen, D., Angot, H., Archer, S., Bariteau, L., Beck, I.,
 Bilberry, J., Bucci, S., Buck, C., Boyer, M., Brasseur, Z., Brooks,
 I., Calmer, R., Cassano, J., Castro, V., Chu, D., Costa, D., Cox,
 C., Creamean, J., Crewell, S., Dahlke, S., Damm, E., Boer, G.,
 Deckelmann, H., Dethloff, K., Dütsch, M., Ebell, K., Ehrlich,

- A., Ellis, J., Engelmann, R., Fong, A., Frey, M., Gallagher, M., Ganzeveld, L., Gradinger, R., Graeser, J., Greenamyer, V., Griesche, H., Griffiths, S., Hamilton, J., Heinemann, G., Helmig, D., Herber, A., Heuzé, C., Hofer, J., Houchens, T., Howard, D., Inoue, J., Jacobi, H.-W., Jaiser, R., Jokinen, T., Jourdan, O., Jozef, G., King, W., Kirchgaessner, A., Klingebiel, M., Krassovski, M., Krumpen, T., Lampert, A., Landing, W., Laurila, T., Lawrence, D., Lonardi, M., Loose, B., Lüpkes, C., Maahn, M., Macke, A., Maslowski, W., Marsay, C., Maturilli, M., Mech, M., Morris, S., Moser, M., Nicolaus, M., Ortega, P., Osborn, J., Pätzold, F., Perovich, D., Petäjä, T., Pilz, C., Pirazzini, R., Posman, K., Powers, H., Pratt, K., Preußer, A., Quéléver, L., Radenz, M., Rabe, B., Rinke, A., Sachs, T., Schulz, A., Siebert, H., Silva, T., Solomon, A., Sommerfeld, A., Spreen, G., Stephens, M., Stohl, A., Svensson, G., Uin, J., Viegas, J., Voigt, C., Gathen, P., Wehner, B., Welker, J., Wendisch, M., Werner, M., Xie, Z., and Yue, F.: Overview of the MOSAiC expedition - Atmosphere, Elementa: Science of the Anthropocene, 10, 00060, https://doi.org/10.1525/elementa.2021.00060, 2022.
- Sigmund, A., Dujarding, J., Comola, F., Sharma, V., Huwald, H., Brito Melo, D., Hirasawa, N., Nishimura, K., and Lehning, M.: Evidence of Strong Flux Underestimation by Bulk Parametrizations During Drifting and Blowing Snow, Bound.-Lay. Meteorol., 182, 119–146, https://doi.org/10.1007/s10546-021-00653-x, 2022.
- Sturm, M. and Holmgren, J.: An Automatic Snow Depth Probe for Field Validation Campaigns, Water Resour. Res., 54, 9695–9701, https://doi.org/10.1029/2018wr023559, 2018.
- Sturm, M. and Massom, R. A.: Snow in the sea ice system: friend or foe?, chap. 3, John Wiley and Sons, Ltd, 65–109, https://doi.org/10.1002/9781118778371.ch3, 2016.
- Sturm, M., Morris, K., and Massom, R.: The Winter Snow Cover of the West Antarctic Pack Ice: Its Spatial and Temporal Variability, in: Antarctic Sea Ice: Physical Processes, Interactions and Variability, edited by: Jeffries, M. O., https://doi.org/10.1029/AR074p0001, 1998a.
- Sturm, M., Morris, K., and Massom, R.: The Winter Snow Cover of the West Antarctic Pack Ice: Its Spatial and Temporal Variability, American Geophysical Union (AGU), 1–18, https://doi.org/10.1029/AR074p0001, 1998b.
- Sturm, M., Holmgren, J., and Perovich, D. K.: Winter snow cover on the sea ice of the Arctic Ocean at the Surface Heat Budget of the Arctic Ocean (SHEBA): Temporal evolution and spatial variability, J. Geophys. Res.-Oceans, 107, SHE 23-1–SHE 23-17, https://doi.org/10.1029/2000JC000400, 2002a.
- Sturm, M., Perovich, D. K., and Holmgren, J.: Thermal conductivity and heat transfer through the snow on the ice of the Beaufort Sea, J. Geophys. Res.-Oceans, 107, SHE 19-1–SHE 19-17, https://doi.org/10.1029/2000JC000409, 2002b.
- Sugiura, K., Yang, D., and Ohata, T.: Systematic error aspects of gauge-measured solid precipitation in the Arctic, Barrow, Alaska, Geophys. Res. Lett., 30, 1192, https://doi.org/10.1029/2002GL015547, 2003.
- Sugiura, K., Ohata, T., Yang, D., Sato, T., and Sato, A.: Application of a snow particle counter to solid precipitation measurements under Arctic conditions, Cold Reg. Sci. Technol., 58, 77–83, https://doi.org/10.1016/j.coldregions.2009.03.010, 2009.
- Toyota, T., Massom, R., Tateyama, K., Tamura, T., and Fraser, A.: Properties of snow overlying the sea ice off East Antarc-

- tica in late winter, 2007, Deep-Sea Res. Pt. II, 58, 1137–1148, https://doi.org/10.1016/j.dsr2.2010.12.002, 2011.
- Trujillo, E. and Lehning, M.: Theoretical analysis of errors when estimating snow distribution through point measurements, The Cryosphere, 9, 1249–1264, https://doi.org/10.5194/tc-9-1249-2015, 2015.
- Trujillo, E., Leonard, K., Maksym, T., and Lehning, M.: Changes in snow distribution and surface topography following a snowstorm on Antarctic sea ice, J. Geophys. Res.-Earth Surf., 121, 2172–2191, https://doi.org/10.1002/2016JF003893, 2016.
- Uttal, T., Curry, J. A., McPhee, M. G., Perovich, D. K., Moritz, R. E., Maslanik, J. A., Guest, P. S., Stern, H. L., Moore, J. A., Turenne, R., Heiberg, A., Serreze, M. C., Wylie, D. P., Persson, O. G., Paulson, C. A., Halle, C., Morison, J. H., Wheeler, P. A., Makshtas, A., Welch, H., Shupe, M. D., Intrieri, J. M., Stamnes, K., Lindsey, R. W., Pinkel, R., Pegau, W. S., Stanton, T. P., and Grenfeld, T. C.: Surface Heat Budget of the Arctic Ocean, B. Am. Meteorol. Soc., 83, 255–276, https://doi.org/10.1175/1520-0477(2002)083<0255:SHBOTA>2.3.CO;2, 2002.
- Vaisala: Present Weather and Visibility Sensors PWD10, PWD12, PWD20, and PWD22 Data Sheet, B210385EN, https://docs.vaisala.com/v/u/B210385EN-F/en-US (last access: 16 June 2022), 2018.
- Vaisala: HMT330 Series Humidity and Temperature Transmitters Datasheet, B210951EN, https://docs.vaisala.com/v/u/B210951EN-S/en-US (last access: 16 June 2022), 2020.
- Wagner, D. N., Jaggi, M., Macfarlane, A. R., Arndt, S., Krampe, D., Regnery, J., Oggier, M., Kolabutin, N., Raphael, I., Shimanchuck, E., and Schneebeli, M.: Snow water equivalent retrievals from SnowMicroPen data from MOSAiC Leg 1–Leg 3, PANGAEA [data set], https://doi.pangaea.de/10.1594/PANGAEA.927460, 2021.
- Wang, C., Graham, R. M., Wang, K., Gerland, S., and Granskog, M. A.: Comparison of ERA5 and ERA-Interim near-surface air temperature, snowfall and precipitation over Arctic sea ice: effects on sea ice thermodynamics and evolution, The Cryosphere, 13, 1661–1679, https://doi.org/10.5194/tc-13-1661-2019, 2019a.

- Wang, D., Bartholomew, M., and Cromwell, E.: Weighing Bucket Precipitation Gauge (WBPLUVIO2), atmospheric Radiation Measurement (ARM) user facility [data set], https://adc.arm.gov/discovery/#/results/datastream:: moswbpluvio2S3.a1 (last access: 16 June 2022), 2019b.
- Webster, M. A., DuVivier, A. K., Holland, M. M., and Bailey, D. A.: Snow on Arctic Sea Ice in a Warming Climate as Simulated in CESM, J. Geophys. Res.-Oceans, 126, e2020JC016308, https://doi.org/10.1029/2020jc016308, 2021.
- Weiss, A. I., King, J., Lachlan-Cope, T., and Ladkin, R.: On the effective aerodynamic and scalar roughness length of Weddell Sea ice, J. Geophys. Res.-Atmos., 116, D19, https://doi.org/10.1029/2011JD015949, 2011.
- Wever, N., Rossmann, L., Maaß, N., Leonard, K. C., Kaleschke, L., Nicolaus, M., and Lehning, M.: Version 1 of a sea ice module for the physics-based, detailed, multi-layer SNOWPACK model, Geosci. Model Dev., 13, 99–119, https://doi.org/10.5194/gmd-13-99-2020, 2020.
- Widener, K., Bharadwaj, N., and Johnson, K.: Ka-Band ARM Zenith Radar (KAZR) Handbook., Tech. rep., aRM user facility, DOE/SC-ARM/TR-106, 2012.
- Wong, K., Fischer, A., and Nitu, R.: Measurement of Precipitation at AWS in Canada: Configuration, Challenges and Alternative Approaches, https://library.wmo.int/pmb_ged/wmo-td_1462_en/P2(12)_Kai_Wong_Canada.pdf (last access: 16 June 2022), 2012.
- Wong, K.: Performance of Several Present Weather Sensors as Precipitation Gauges, in: WMO TECO, 16–18 October 2012, Brussels, Belgium, 25 pp., https://library.wmo.int/pmb_ged/iom_109_en/Session1/P1_30_
- Wong_Performance_Wx_Sensors_Precip_Gauges.pdf (last access: 16 June 2022), 2012.